Kent Academic Repository

Bhachu, Tanveer S. and Smith, Michael D. (2026) ***Magnetohydrodynamic flow patterns in high-pressure jet exhausts containing toroidal fields.*** **Monthly Notices of the Royal Astronomical Society, 548 (4). ISSN 0035-8711.**

Monthly Notices
of the
ROYAL ASTRONOMICAL SOCIETY

MNRAS **548,** 1–19 (2026)
Advance Access publication 2026 April 17

https://doi.org/10.1093/mnras/stag725

Magnetohydrodynamic flow patterns in high-pressure jet exhausts containing toroidal fields

Tanveer S. Bhachu[1]⋆ and Michael D. Smith [1,2]⋆

[1] Centre for Astrophysics & Planetary Science, The University of Kent, Canterbury, Kent CT2 7NH, UK
[2] Department of Physics, Amrita School of Physical Sciences, Amrita Vishwa Vidyapeetham, Amritapuri Campus, Kollam, Kerala 690525, India

Accepted 2026 April 7. Received 2026 March 30; in original form 2025 December 10

ABSTRACT

A magnetic field is generally present within astrophysical jets. Constraining the field properties just as the jet emerges may help to understand the principles behind jet propagation and jet feedback into their surroundings. Taking an adiabatic, supermagnetosonic flow in which the field is frozen-in provides a set-up in which the flow characteristics depend mainly on the jet pressure, Mach number and relative magnetic field strength. To perform numerical simulations we also take a uniform density and implement a toroidal field. We distinguish conditions which generate Mach shock discs rather than a diamond pattern of oblique regular reflections. Some diagnostics that were explored included the shock pattern, the flow pattern, shock stand-off distance from the nozzle, velocity sheath, and oscillations in shock positions. Rapid oscillations occur in the divergent-convergent pattern through a feedback/hysteresis effect promoted by the ambient medium only for a passive field. Slow, high-amplitude variations are promoted by back-flow in a variable cocoon flow. We also study the energy transferred into the environment. Overpressured jets may contribute to noise and sound wave generation through screeching and droning. However, these oscillations that are due to the near-field are shown to be sufficiently unlikely to regulate star and galaxy formation. Overall, the major consequence reported here is that a toroidal field alters the shape of jet knots from diamonds to elongated prolate lenses.

Key words: magnetohydrodynamics – shock waves – stars: jets.

1 INTRODUCTION

Magnetic fields can be responsible for propelling and collimating astrophysical jets from protostars and galactic nuclei (R. E. Pudritz, M. J. Hardcastle & D. C. Gabuzda 2012; M. D. Smith 2012) as well as being utilized for gas acceleration in rocket engines (V. Pulatov 2001). The observed jets themselves are collimated regions of high energy transport in which strong shocks and other dynamical processes can be studied. High pressures may be encountered and in some cases the jets may be overpressured generating shocks (S. Mandal, P. C. Duffell & Y. Li 2022; V. Velović et al. 2022). Ideally, we can analyse these observations and determine the precise role played by the magnetic field. However, to do so we need to get familiar with the differences encountered between purely hydrodynamic (HD) models and their magnetohydrodynamic (MHD) counterparts.

Here we systematically search for the signatures which we can attribute to MHD flows in the region where an overpressured jet flow expands and contracts on leaving a circular nozzle. Two specific patterns of shock waves are predicted when overpressured, supersonic jets are released from a nozzle. A diamond pattern, also termed regular reflection, is a series of oblique shocks at low overpressures (R. Bonito et al. 2011). At the opposite extreme, a strong perpendicular shock front called a Mach shock disc or Mach disc, intercepts the flow for high overpressures. The flow pattern is also referred to as Mach reflection. In this case an incident oblique shock meets and reflects off the Mach disc at a triple point or circle above the jet axis (E. Franquet et al. 2015; M. D. Smith & T. L. R. Keogh 2022; T. Hanawa et al. 2025).

Three basic non-dimensional numbers are involved. The relative magnetic field strength, represented here by the parameter σ, is one such number. M. D. Smith & C. Richards (2023) demonstrated that there are just two primary parameters that specify the flow pattern in the HD case. These are the jet Mach number, $M_{\rm jet}$, and overpressure, κ, with a division at roughly $\kappa \propto M_{\rm jet}$ at high $M_{\rm jet}$ with overpressures above this value more likely to involve Mach discs. Our goal here is to explore these three dimensionless numbers. However, it should be noted that there is no precise division and several hybrid possibilities and oscillatory flows can occur.

This line of research is complementary to the latest high-resolution observations which confirm the detections of stationary shock configurations (T. G. Arshakian et al. 2024; Y.-R. Chou et al. 2025). This suggests scenarios in which the jets diverge and converge as a reaction and over-reaction to the pressure

---

⋆ E-mail: m.d.smith@kent.ac.uk (MDS); tsb24@kent.ac.uk (TSB)

mismatch. If true, we can learn from the recollimation not only about the physics of jets but also the properties of the driving source and the nature of the environment.

Laboratory experiments have been mainly motivated by astrophysical jets. A Biermann batttery-induced field was created by W. Fu et al. (2015) with a field energy of 10^{-4} of the thermal energy. Hence, the field has little effect on the dynamics. Here, we include this model with a similar strength passive field. A plethora of experiments have followed although there is no systematic development. For example, Z. Lei et al. (2024) demonstrated that a static toroidal field would confine a jet. It is clear that a systematic approach is needed to assess the relevance in terms of flow and shock patterns. A second major issue to contend with is the jet driving mechanism. As with the outflow production of F. Suzuki-Vidal et al. (2011), the set-up is not force free, leading to the generation of current reconnection events, multiple magnetic cavities and an unstable jet.

The alternative approach is through simulations in which the injected jet and field can be manipulated. As will also be studied in this work, we can simulate MHD jets based on adiabatic non-relativistic flows with imposed axisymmetry. A preliminary numerical study took a dominant toroidal field (D. A. Clarke, M. L. Norman & J. O. Burns 1986). This field increased linearly from zero on the axis with a value of the plasma $\beta = 0.2$ at the boundary corresponding to a constant current density. The jet thermal pressure matched the ambient thermal pressure with a Mach number of 6.0. In contrast, this implies that there was an inherent force imbalance due to the magnetic tension which resulted in pinching and internal shocks.

An approach in which a jet begins in a force-free configuration may provide more insight. This was achieved by K. R. Lind et al. (1989) taking a thermal pressure gradient to balance the magnetic forces in the core of the jet. This inner jet was taken with a uniform speed and current density. The result was a linearly increasing magnetic field in the radial direction. Secondly, a coaxial outer jet of constant thermal pressure was used where no current was added. Hence, the magnetic field falls inversely with the radius such that the magnetic tension and magnetic pressure are in balance. Finally, the field drops to zero across the jet boundary which is the location of the back-flowing current. This profile has subsequently been adopted by many others including E. C. Hansen, A. Frank & P. Hartigan (2015) and Y. Mizuno et al. (2015). The analyses usually assume a pressure equilibrium across the interface taking into account the additional magnetic pressure difference exerted across it. Here we apply an overpressure commensurate with our HD results by setting the overpressure as the ratio of the jet to ambient thermal pressures across the interface.

Overpressured magnetized jets have already received attention. Y. Mizuno et al. (2015) fixed the overpressure to 1.5 and thus studied non-equilibrium jets at low overpressure. They found that an axial field effectively adds to the overpressure amplifying the shock pattern while a toroidal field weakens the shocks consistent with the lack of an outer counterpressure. J. M. Martí, M. Perucho & J. L. Gómez (2016) also used a low overpressure which limited the shock strengths in models dominated by the kinetic energy. In this case, high internal energies were needed to create a rich and variable jet structure.

Now we investigate a wide range in overpressures. High overpressures would also lead to rich internal shock structures and thus we need other signatures to differentiate between HD and MHD models. We do however limit this initial study to non-relativistic jets containing a toroidal field. We also do not consider opening angles and rotation among other model variations which would affect the shock structure and variability. Finally, we eliminate the possible contribution of normal or torsional Alfvén waves propagating along the jet (M. H. Cohen et al. 2015) by the lack of a poloidal field component.

The jet thermal pressure and sound speed is no longer constant over the cross-section and so we have to pay attention to the definition of jet Mach number. As a replacement for this Mach number, we employ the jet speed and the jet sound speed on the jet axis. With a toroidal field, the field strength is zero on this axis and therefore the magnetosonic and sound speeds are equal. By fixing this value to 2.0, we can compare directly to results for HD jets as per M. D. Smith & T. L. R. Keogh (2022, hereafter referred to as SK22).

In the near field, while still axisymmetric, we assume that cylindrical symmetry is appropriate. Further downstream, fluid and MHD instabilities need to be discussed and 3D simulations eventually become necessary.

Besides the origin of the jet, we are interested in how it interacts with the environment to provide positive or negative feedback that could be ultimately related to many evolutionary scenarios involving regulation and triggering (S. Rawlings & M. J. Jarvis 2004; S. Hillel, R. Schreier & N. Soker 2022). We therefore wish to determine how much energy continues to be poured into the surroundings in the form of noise, turbulence and heat.

This study builds on the HD case where $M_{jet} = 2.0$ as in the analysis of SK22. The injected jet was uniform and circular with constant density and speed. The gas was adiabatic with specific heat ratio of $\gamma = 5/3$ and the jet began as perfectly collimated. Chemistry, cooling, gravity and relativistic effects were not included thus additional physics as well as dynamics such as pulses, bursts, spray, precession and shear were not considered. Major results that we wish to extend here include the following:

1. The flow pattern near the nozzle settles towards a quasi-steady configuration in the long term. This was confirmed through space-time diagrams which show the initial period in which the jet working surface advances far downstream.

2. High-density jets generate quite steady channels and shock patterns with slow oscillations. Light jets also settle down except for high overpressures which continue to oscillate with high amplitude.

3. Two extremes to the flow patterns were discussed. At low overpressures, a diamond shock pattern which involves intersecting oblique shocks occurs. At high overpressures, a normal Mach disc intercepts the oblique shocks due to the wide divergent-convergent structure.

4. At intermediate overpressures, a series of Mach discs can occur downstream of the stand-off shock while at high overpressures a turbulent plume is predicted.

5. The oscillations drive sound waves into the ambient medium. A lateral dispersion of energy occurs in some cases. However, a major effect of this sloshing is to promote the advection of ambient gas away from the nozzle and draw more material towards the jet axis.

This paper leads on from these results with the added toroidal magnetic field. Other spin-offs have now included a study of the dependence on Mach number (M. D. Smith & C. Richards 2023), velocity pulses of various frequencies (C. Richards & M. D. Smith 2024) and the transition from regular to Mach reflection as the jet opening angle increases (M. D. Smith et al. 2025).

Table 1. The parameters defining the jet and ambient medium.

Parameter	Pressure	Density	Specific heat ratio	Sound speed	Velocity	Mach number	Toroidal field
Ambient medium	$p_{\rm amb}$	$\rho_{\rm amb}$	γ	$c_{\rm amb}$	$v_{\rm amb}$	$M_{\rm amb} = v_{\rm amb}/c_{\rm amb}$	$B_{\rm amb}$
Ambient medium value	0.6	1	5/3	1	0	0	0
Jet ($r = R_m$)	$p_{\rm jet} = \kappa \times p_{\rm amb}$	$\rho_{\rm jet} = \eta \times \rho_{\rm amb}$	γ	$c_{\rm jet}$	$v_{\rm jet}$	$M_{\rm jet} = v_{\rm jet}/c_{\rm jet}$	B_m
Jet ($r = 0$)	$p_{\rm jet} = \kappa \times p_{\rm amb} + B_m^2$	$\rho_{\rm jet} = \eta \times \rho_{\rm amb}$	γ	$c_{\rm s,axis}$	$v_{\rm jet}$	$M_{\rm jet} = v_{\rm jet}/c_{\rm s,axis}$	0

2 METHOD

2.1 The code and boundary conditions

The simulations were performed with *PLUTO*, a grid-based code incorporating Godunov-type shock-capturing schemes. This code is freely-distributed (A. Mignone et al. 2007) .[1]

The MHD equations of ideal gases are evolved. Two-dimensional (2D) axial symmetry is taken with radial and axial velocity components. The flow enters from a circular hole in a wall. The other boundaries are those of free outflow as is always taken for jet and radio galaxy simulations to avoid reflection of sound and shock waves.

The application of ideal MHD to a jet problem requires justification. The transition from the kinetic scale in which a variety of plasma processes are important to the MHD scale is crucial at shock fronts and shear layers in jets. That is where a particle-in-cell (PIC) code (e.g. B. Cerutti & G. Giacinti 2023) performs better. Here, we follow an ideal MHD treatment noting that this assumes all viscous effects are confined to narrow boundary layers and shock fronts. We also ensure MHD equilibrium as the jet exits the nozzle. The toroidal field would pinch the jet if there was no counter thermal pressure gradient introduced to balance the inward net magnetic force. As the jet gas propagates downstream, it cannot remain force free due to the overpressure. However, the field remains toroidal in axisymmetric simulations and the current remains poloidal.

We choose only toroidal magnetic fields and also restrict the analysis to the inner jet where kink instabilities (e.g. J. Davelaar et al. 2020) would remain in the linear regime.

The primitive form of the MHD equations, neglecting diffusion terms, are given by

$$\frac{\partial \rho}{\partial t} + v{\cdot}\nabla\rho + \rho\nabla\cdot v = 0, \tag{1}$$

$$\frac{\partial v}{\partial t} + v\cdot\nabla v + \frac{1}{\rho}B\times(\nabla\times B) + \frac{1}{\rho}\nabla p = -\nabla\Phi + \mathrm{g}, \tag{2}$$

$$\frac{\partial B}{\partial t} + B(\nabla\cdot v) - (B\cdot\nabla)v + (v\cdot\nabla)B = v(\nabla\cdot B), \tag{3}$$

$$\frac{\partial \rho}{\partial t} + v\cdot\nabla p + \rho c_s^2\nabla\cdot v = 0, \tag{4}$$

where ρ is the density, v is the velocity, B is the magnetic field strength, p is the pressure, Φ represents the gravitational potential, g is the gravitational acceleration, and c_s denotes the sound speed.

After doing some tests, we found optimal results for simulations using a Courant–Friedrichs–Lewy value of 0.4 and a simple Total Variable Diminishing Lax–Friedrichs (TVDLF) Riemann solver for computing fluxes.

Simulations were run up to 200 time units allowing enough time for the system to settle down and display any underlying shock patterns. Here we define a time unit in terms of the jet radius, $R_{\rm jet}$, and the ambient sound speed, $c_{\rm amb}$, as per $t_u = R_{\rm jet}/c_{\rm amb}$.

The simulations were performed on uniform cylindrical grids of 200 radially distributed zones and $200M_{\rm jet}$ zones along the jet axis where $M_{\rm jet}$ is the jet Mach number. This converts into $10R_{\rm jet}$ and $20M_{\rm jet}R_{\rm jet}$, respectively. Hence, the length of the grid is proportional to the Mach number, anticipating that the flow pattern will be stretched to some extent.

In addition, a vast reservoir is required to allow the pressure disturbances to freely propagate outwards without being influenced by the domain boundary. This must hold for the long duration of these experiments. Therefore, extended regions of zones stretched in a geometric series of number 100 × 200 were added in the radial and axial directions to take the full grid domain to $60R_{\rm jet}$ radially and $(100 + 10M_{\rm jet})R_{\rm jet}$ on the jet axis.

To display and analyse the results, we use IDL software programmes. Images display cross-sections, reflected about the jet axis to aid interpretation. Only the uniform sections are shown unless stated otherwise.

2.2 The scaling

The simulations are dimensionless and so can be scaled for any adiabatic inviscid gas. Table 1 defines physical parameters with the two major HD ones being the pressure and density ratios across the jet, boundary at the nozzle:

$$\kappa = \frac{p_{\rm jet}}{p_{\rm amb}}, \tag{5}$$

$$\eta = \frac{\rho_{\rm jet}}{\rho_{\rm amb}}. \tag{6}$$

We set up our units in terms of the jet radius, $R_{\rm jet} = 1$, and the ambient sound speed, $c_{\rm amb} = 1$. Hence, the unit of time is $t_u = 1$.

Taking the ambient density $\rho_{\rm amb} = 1$ then fixes the ambient pressure as

$$p_{\rm amb} = \frac{\rho_{\rm amb}c_{\rm amb}^2}{\gamma}. \tag{7}$$

This yields a pressure $p_{\rm amb} = 1/\gamma = 0.6$ and internal energy per unit volume $u_{\rm amb} = 0.9$ for the specific heat ratio of $\gamma = 5/3$ since

$$u_{\rm amb} = \frac{p_{\rm amb}}{\gamma - 1}. \tag{8}$$

The jet enters from the lower-z boundary from a circular nozzle of radius $R_{\rm jet}$ and carries a constant poloidal field B_z and a (radially-varying) toroidal component $B_\phi(r)$.

The flow variables are prescribed as

$$\begin{aligned} \rho(r) &= \rho_{\rm jet} \\ v_z(r) &= v_{\rm jet} \\ B_z(r) &= B_{z,0} \quad \text{(const).} \end{aligned}$$

$$B_\phi(r) = \begin{cases} -B_m r/R_m & \text{for} \quad r < R_m, \\ -B_m R_m/r & \text{for} \quad r > R_m, \end{cases} \tag{9}$$

---

[1] `http://plutocode.ph.unito.it/`

following K. R. Lind et al. (1989). In the formulae below, we substitute $R_m/R_{\rm jet} = a$ for the magnetization radius which is where the field reaches a peak value of B_m for the toroidal field component.

The pressure across the entering jet is assumed to have evolved to achieve a force-free distribution. It is found by solving the radial momentum balance between centrifugal, magnetic and thermal forces that

$$\frac{{\rm d}p}{{\rm d}R} = \frac{\rho v_\phi^2}{R} - \frac{1}{2}\left[\frac{1}{R^2}\frac{{\rm d}(R^2B_\phi^2)}{{\rm d}R} + \frac{{\rm d}B_z^2}{{\rm d}R}\right]. \qquad (10)$$

In this initial study we take $v_\phi = 0$ and $B_z = 0$. Note also that $v_r = B_r = 0$. These profiles are similar to the ones used previously (O. Teşileanu, A. Mignone & S. Massaglia 2008).

It follows that, neglecting rotation and assuming B_z to be constant, the solution to the radial momentum balance becomes

$$p(r) = \kappa p_a + B_m^2\left[1 - \min\left(\frac{r^2}{R_m^2}, 1\right)\right], \qquad (11)$$

which corresponds to a constant pressure outside the magnetization radius where the forces due to magnetic pressure and magnetic tension cancel each other out.

The jet on-axis pressure increases for increasing toroidal field as

$$p(r=0) \equiv p_j = \kappa \times p_{\rm amb} + B_m^2 \qquad (12)$$

where $p_{\rm amb}$ is the ambient pressure and κ is the thermal overpressure at $R_{\rm jet}$.

The relative field is defined by the poloidal magnetization, σ_z, and the toroidal magnetization, σ_ϕ. These magnetization parameters are defined as

$$\sigma_z = \frac{B_{z,0}^2}{2p_{\rm amb}}, \qquad (13)$$

$$\sigma_\phi = \frac{< B_\phi^2 >}{2\kappa\, p_{\rm amb}}. \qquad (14)$$

Here, the axial field is defined, as in previous studies, in terms of the ambient pressure. However, the azimuthal component is now modified to be relative to the jet pressure. As seen below, this eases an analysis in terms of the relative magnetic field within the jet.

On setting $a = R_m/R_{\rm jet}$ this yields

$$B_m^2 = \frac{2\sigma_\phi}{a^2(0.5 - 2\ln a)} p_{\rm jet}. \qquad (15)$$

Here, the average value of B_ϕ^2 is simply found as

$$< B_\phi^2 > = \frac{\int_0^1 B_\phi^2 R\,{\rm d}R}{\int_0^1 R\,{\rm d}R} = B_m^2 a^2\left(\frac{1}{2} - 2\ln a\right). \qquad (16)$$

We can fully define a flow pattern in terms of seven non-dimensional numbers. In this work, five of these are fixed as firstly we take $a = 0.8$ remembering that $\gamma = 5/3$. We also take the magnetic field to be purely toroidal, setting $\sigma_z = 0$. This is an assumption often made more out of interest than expectation or observation (D. A. Clarke et al. 1986) with toroidal magnetic confinement in fusion technology being a long-standing problem. However, simple flux-freezing arguments within a uniform jet would suggest that the toroidal field would become dominant on large scales in the absence of shear or turbulence (M. D. Smith 2012).

We also take a light jet with $\eta = 0.1$ noting that the chosen density ratio is not significant provided a steady flow pattern is achieved in which only the pressure across the interface determines the flow. However, the density should also be considered when feedback and surface waves disturb the flow.

Finally, we remind ourselves that the Mach number of the jet on the axis is $M_{\rm jet} = 2.0$. This is set in order to make all our results directly comparable to the purely HD results of SK22.

Two parameters remain: the overpressure and the relative magnetic field strength within the jet. These are used to determine the correct value for $v_{\rm jet}$ using a conversion of

$$v_{\rm jet} = M_{\rm jet} \times c_{\rm s,axis} = 2.0 \times \sqrt{\frac{\kappa(1.0 + 3.30238\sigma_\phi)}{\eta}} \qquad (17)$$

on substituting the above parameters, where $c_{\rm s,axis}$ is the sound speed on the jet axis and σ_ϕ is a parameter used to initialise the toroidal field component.

In order to generate a toroidal field we used asymmetrical cylindrical geometry with a uniform ambient medium at rest. As the jet enters the stationary medium from the nozzle, it carries a radially-varying toroidal field. Therefore B_m is defined as

$$B_m = \sqrt{\frac{1.2\sigma_\phi\kappa}{a^2(0.5 - 2\ln a)}} \qquad (18)$$

with $a = 0.8R_{\rm jet}$ being a scale length and $\kappa = p_{\rm jet}/p_{\rm amb}$ is the jet-ambient medium pressure ratio. Given that the sound speed on the jet axis is $c_{\rm s,axis} = \sqrt{(\kappa + \gamma B_m^2)/\eta}$ where $\eta = \rho_{\rm jet}/\rho_{\rm amb}$ is the jet-ambient medium density ratio. Thus, when we combine these with equation (18) we arrive at equation (17) defining the jet speed as before.

In summary, four parameters are needed to fully run a simulation. These are the pressure ratio, κ, density ratio, η, jet velocity (adiabatic set-up), $v_{\rm jet}$, and the toroidal magnetic field component, σ_ϕ. In our study, we take the case of light, overpressured and supersonic jets ($\eta = 0.1$, $M_{\rm jet} = 2$) with a range of pressure ratios, κ, as well as toroidal field strengths, σ_ϕ, as per Table 2.

Six quantities are recorded to file at each of 1000 data dumps separated by $0.2t_u$ allowing evolution over $200t_u$. The quantities are the density, ρ, pressure, p, two velocity components, v_z (axial velocity) and v_r (radial velocity), mass-weighted jet tracer, χ, and the toroidal field strength, B_ϕ.

Note that the tracer records the relative amount of gas in each zone that entered from the nozzle and may now lie in the jet, cocoon, or stagnant vortices.

To provide insight into the set-up of the boundary conditions, we present radial profiles of the physical parameters at the plane containing the nozzle and wall at $z = 0$. Figs 1 and 2 demonstrate the profiles for a highly overpressured jet.

The upper panel of Fig. 1 confirms the weak azimuthal (i.e. toroidal) magnetic field distribution in the jet with no induced poloidal components evident. The lower panel shows that the thermal pressure has reached equilibrium (solid line) with the passive field, as in the purely HD flow. However the external gas has been heated with the density reduced from the initial ambient value of unity.

Imposing a strong azimuthal field, the field distribution remains unaltered as confirmed in the upper panel of Fig. 2. However, the thermal pressure is now strongly centrally peaked (solid line in lower panel). Hence, the sound speed in the jet reaches a maximum on the axis where the field is absent. External to the

Table 2. The range of values taken for $v_{\rm jet}$ given a range in κ and σ_ϕ to initialise a simulation. These values are calculated to 3sf using equation (17) with a Mach number of 2.0 on the jet axis where the magnetic field is absent. All quantities are in simulation units. Blank entries are where no simulation was run.

	$\sigma_\phi = 10^{-4}$	$\sigma_\phi = 0.125$	$\sigma_\phi = 0.25$	$\sigma_\phi = 0.5$	$\sigma_\phi = 0.75$	$\sigma_\phi = 1$	$\sigma_\phi = 2$	$\sigma_\phi = 4$
$\kappa = 2$	8.95	10.6	12.1	14.6	16.7	18.6	24.7	33.7
$\kappa = 4$	12.7	15.0	17.1	20.6	23.6	26.2	34.9	47.9
$\kappa = 6$	15.5	18.4	20.9	25.2	28.9	32.1	42.7	58.4
$\kappa = 8$	17.9	21.3	24.2	29.1	33.4	37.1	49.3	67.4
$\kappa = 10$	20.0	23.8	27.0	32.6	37.3	41.5	55.2	75.4
$\kappa = 12$	21.9	26.0	29.6	35.7	40.9	45.4	60.4	82.6
$\kappa = 14$					44.1	49.1	65.3	89.2
$\kappa = 16$					47.2	52.5	69.8	95.4
$\kappa = 18$					50.0	55.7	74.0	101.1
$\kappa = 20$					52.7	58.7	78.0	106.6

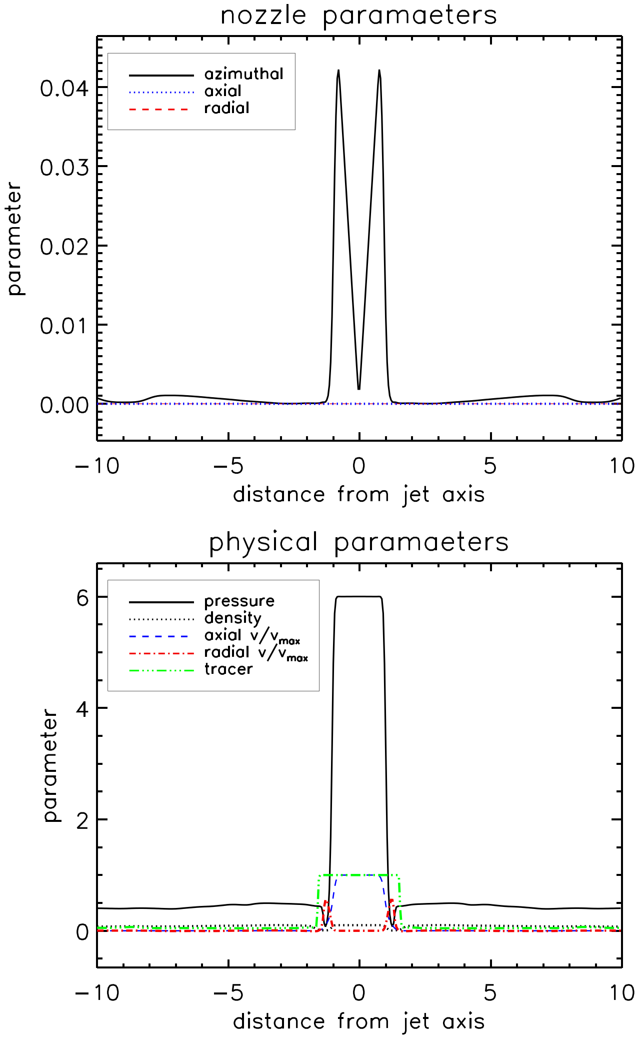

Figure 1. Inflow boundary: passive toroidal field with high over-pressure. The physical and magnetic field parameters across the inflow boundary at the end of the simulation with a time of $t = 200t_u$ for $\sigma_\phi = 10^{-4}$ and $\kappa = 10$. The velocities are normalized to the maximum velocity of $v_{\max} = 20.003$ to 3dp for ease of display.

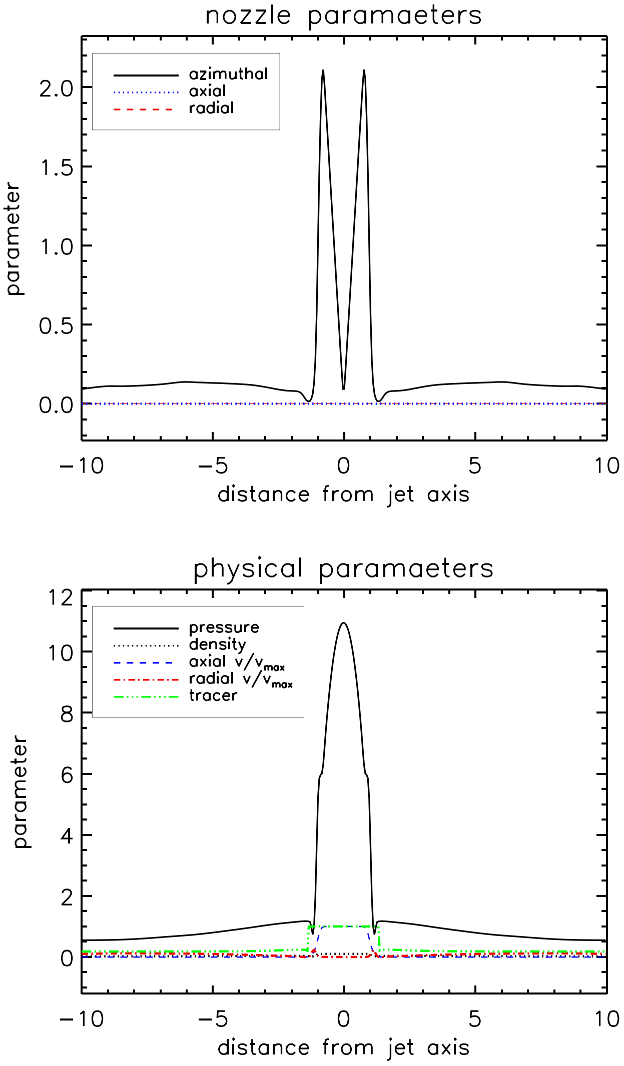

Figure 2. Inflow boundary: moderate toroidal field with high over-pressure. The physical and magnetic field parameters across the inflow boundary at the end of the simulation with a time of $t = 200t_u$ for $\sigma_\phi = 0.25$ and $\kappa = 10$. The velocities are normalized to the maximum velocity of $v_{\max} = 27.023$ to 3dp for ease of display.

jet, a backflow of jet gas in the cocoon has filled a stagnant layer of warm gas adjacent to the wall.

3 NEAR-PASSIVE MAGNETIC FIELD

We first demonstrate the flow patterns revealed when a very low magnetic field is incorporated. The left-hand side panels of Fig. 3 display the toroidal field and physical parameters for $\sigma_\phi = 10^{-4}$. Such a field is termed 'passive' since it will have negligible influence on the HD shock patterns in the absence of a toroidal field as presented by SK22.

Fig. 3 displays the structure for a mild overpressure, $\kappa = 2$, where the sub-panels are appropriate for the analysis of this matter. In particular, the lower-right panel displays the pressure cross-section which best highlights the shock fronts. The tracer in the lower-left panel follows the mass-weighted gas where jet material is allotted the value of 1.0 while the ambient material is 0.0. For display purposes, a minimum of 10^{-3} is shown in the log-tracer panel.

The distribution of the toroidal field does not directly follow the physical parameters but appears similar to that of the density. One notices that the field can be higher within a vortex ring of jet material that has been trapped in the ambient medium. Given the toroidal field with axial symmetry, there is no gas flow along field lines and so the magnetic field is proportional to the density of gas originating from the jet.

For a moderate overpressure, the distributions are quite different. The left side of Fig. 4 shows that a Mach disc arises when $\kappa = 4$. This stand-off shock front pattern replaces the regular reflection of Fig. 3 that occurs at low overpressures. This follows our expectations from HD simulations since the magnetic field is dynamically passive. We then expect a transition from regular reflection to a Mach disc to occur at $\kappa = 3.5$ (SK22). However, at this intermediate stage, the Mach disc is confined to a spine while a fast sheath is sustained.

Sharp spikes are prominent in the magnetic field, emanating from the stand-off Mach disc, into the fast jet sheath. The passive magnetic field in Fig. 4 displays the spikes corresponding to jet density enhancements at the oblique reflected shocks. This may prove to be a significant diagnostic with a high thermal pressure also coincident (lower right sub-panel).

At high overpressures, as shown on the left-side panels of Fig. 5, the Mach disc cuts across the jet but the subsequent flow is dominated by a high pressure slow spine with a narrow fast sheath. Fig. 5 is for an overpressure of $\kappa = 8$. It demonstrates that the thermal pressure can jump by almost two orders of magnitude at a Mach disc but the magnetic field follows the density which increases by at most ~ 4 for a specific heat ratio of 5/3.

In addition, the jet has a greater effect on the surroundings blowing out much of the ambient medium. The jet is still mainly encompassed by ambient gas, as evidenced by the tracer, but it is at a low density and high temperature. A smooth field distribution is present instead of the vortex rings. At even higher κ, a turbulent plume ensues which requires three-dimensional (3D) calculations to accurately simulate.

In summary, the field follows the density distribution. This is clearly seen in the $\kappa = 4$ simulations. Close inspection yields that this structure is present in the density distribution also. Hence, the interpretation is that the frozen-in field is compressed within the flow in proportion to the density and so does not experience the same entropy/pressure jumps associated with the gas shocks.

4 STRONG MAGNETIC FIELD

4.1 Flow patterns

In the case of a strong field, the equivalent final flow configurations are displayed on the right-hand side of Figs 3 – 5. In order to ensure that the inflow speed remains supermagnetosonic across the entire jet, we have chosen to hold the axial Mach number to lie well within the supersonic regime. We do not set it too high in order to better explore the flow patterns. We expect to be able to extrapolate to high Mach numbers as was achieved in the analysis of M. D. Smith & C. Richards (2023). Setting $M_{\rm jet} = 2.0$ in equation (17) then yields the jet inflow speed. These values are listed in Table 2.

The first shock on the axis downstream of the nozzle, the stand-off shock, can be classified as either a regular reflection or a Mach disc. In the case of passive fields, the repetitive diamond pattern of regular reflection occurs only for overpressures below ~ 3.5. We show here that raising the magnetic field while holding the axial Mach number constant, results in regular reflection to higher overpressures. Note that the overpressure is that of the initial jet thermal pressure across the boundary with the undisturbed ambient medium. The axial pressure is much higher so to counter the squeezing due to the magnetic tension. The toroidal field also restrains the jet divergence which permits oblique shocks to be adequate to reflect the converging flow.

As simulations were performed with dynamically active magnetic fields we find that Mach discs still occur but require high thermal overpressures. Precise transition parameters are difficult to ascertain and, as shown below, are likely to be time dependent. Having run simulations in steps of κ of 2, Mach discs (MD) are distinct at and above the following values:

$\kappa > \kappa_{\rm MD}$ with
$\kappa_{\rm MD} = 4$ for $\sigma_\phi = 10^{-4}$,
$\kappa_{\rm MD} = 6$ for $\sigma_\phi = 0.125$,
$\kappa_{\rm MD} = 10$ for $\sigma_\phi = 0.25$,
$\kappa_{\rm MD} = 12$ for $\sigma_\phi = 0.5$,
$\kappa_{\rm MD} = 14$ for $\sigma_\phi = 0.75$.

Observationally, we can usually detect a jet as a chain of bright knots superimposed on a noisy background. It is therefore of interest to classify the chains here according to the shock pattern. We leave the full production of emissivity and surface brightness distributions to a following work.

Six chain patterns can be identified in simulations. These are denoted (a) to (f) and tabulated in Table 3 and are as follows:

(i) Regular diamond reflection chain,
(ii) Regular ovoid oblique chain,
(iii) Regular ovoid followed by Mach disc chain,
(iv) Series of Mach discs,
(v) Mach disc followed by sheath, and
(vi) Mach disc followed by turbulent plume.

These patterns were illustrated by M. D. Smith et al. (2025) having been identified in simulations in which the jet opening angle was the parameter varied. As the nozzle opening angle was increased, the flow pattern shifted from (a) towards (f). Here, from Table 3 it is evident that a toroidal field has the reverse effect. As the relative field strength is increased, the flow pattern alters from (f) to (a) for fixed κ.

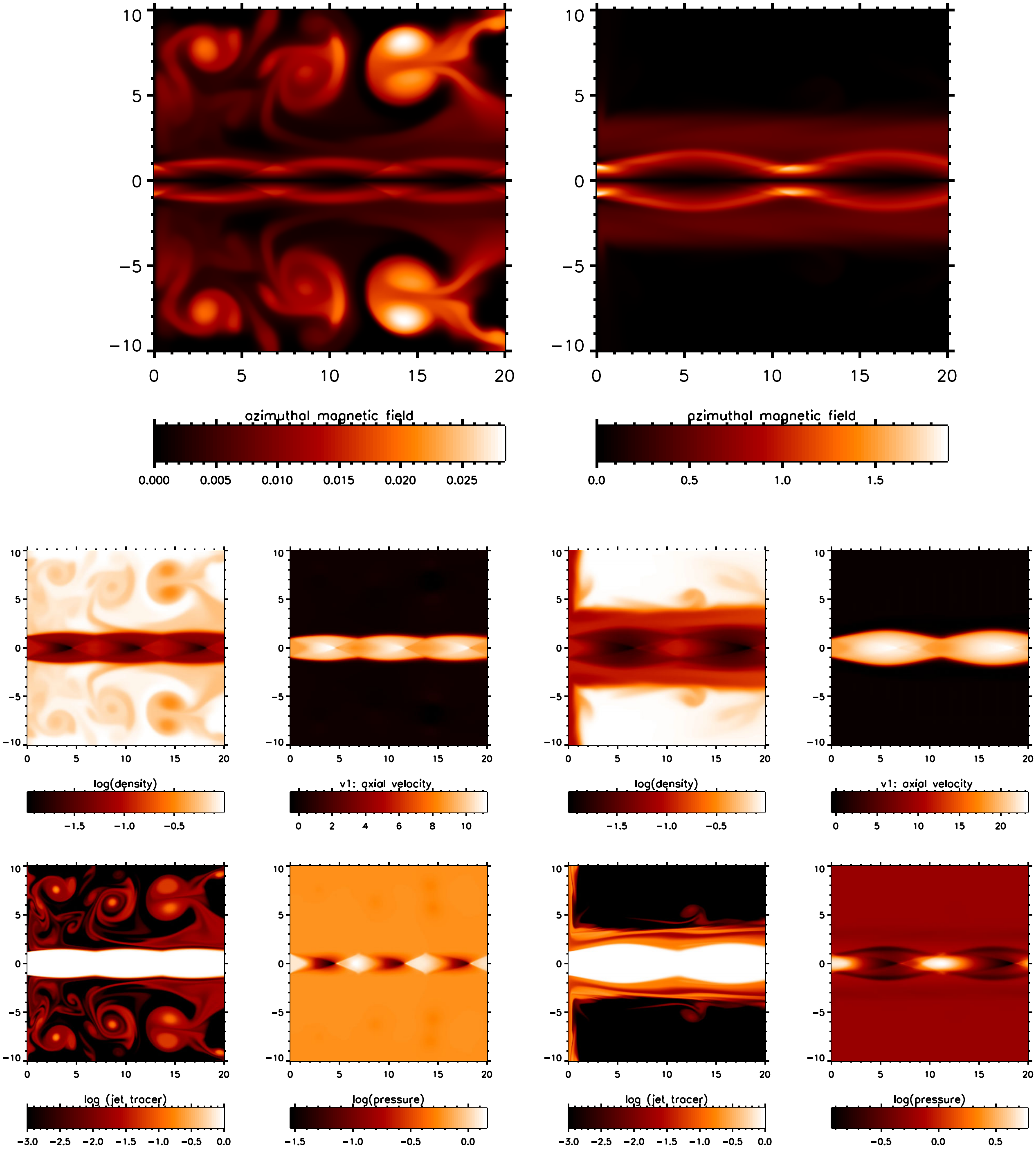

Figure 3. Passive (left) and active (right) fields at a low jet overpressure. The distributions of toroidal magnetic field (top panels) and physical parameters (lower sub-panels) for $\kappa = 2$ and a passive field with $\sigma_\phi = 10^{-4}$ as well as a strong field with $\sigma_\phi = 1$. The time corresponds to the end of the simulation at $t = 200t_u$. The length scale is in units of the jet radius. Upper-left sub-panel: density, upper-right sub-panel: axial velocity, lower-left sub-panel: tracer for jet gas and lower-right sub-panel: pressure.

4.2 New structure

Prominent short arcs of toroidal fields are generated within the wings of the well collimated jets shown on the right-hand side of Figs 3–5. The arcs are in the jet but associated external to the diamond structure of the thermal pressure adding to the pinching effect already present without a strong field.

More striking is the disappearance of the vortex rings in the surrounding medium. The vortices are absent in the density, tracer and magnetic field. Instead, a weak diffuse field encompasses the jet. The origin of this is surmized from the jet tracer to be the leftover overspill from the original jet advancement on to the grid.

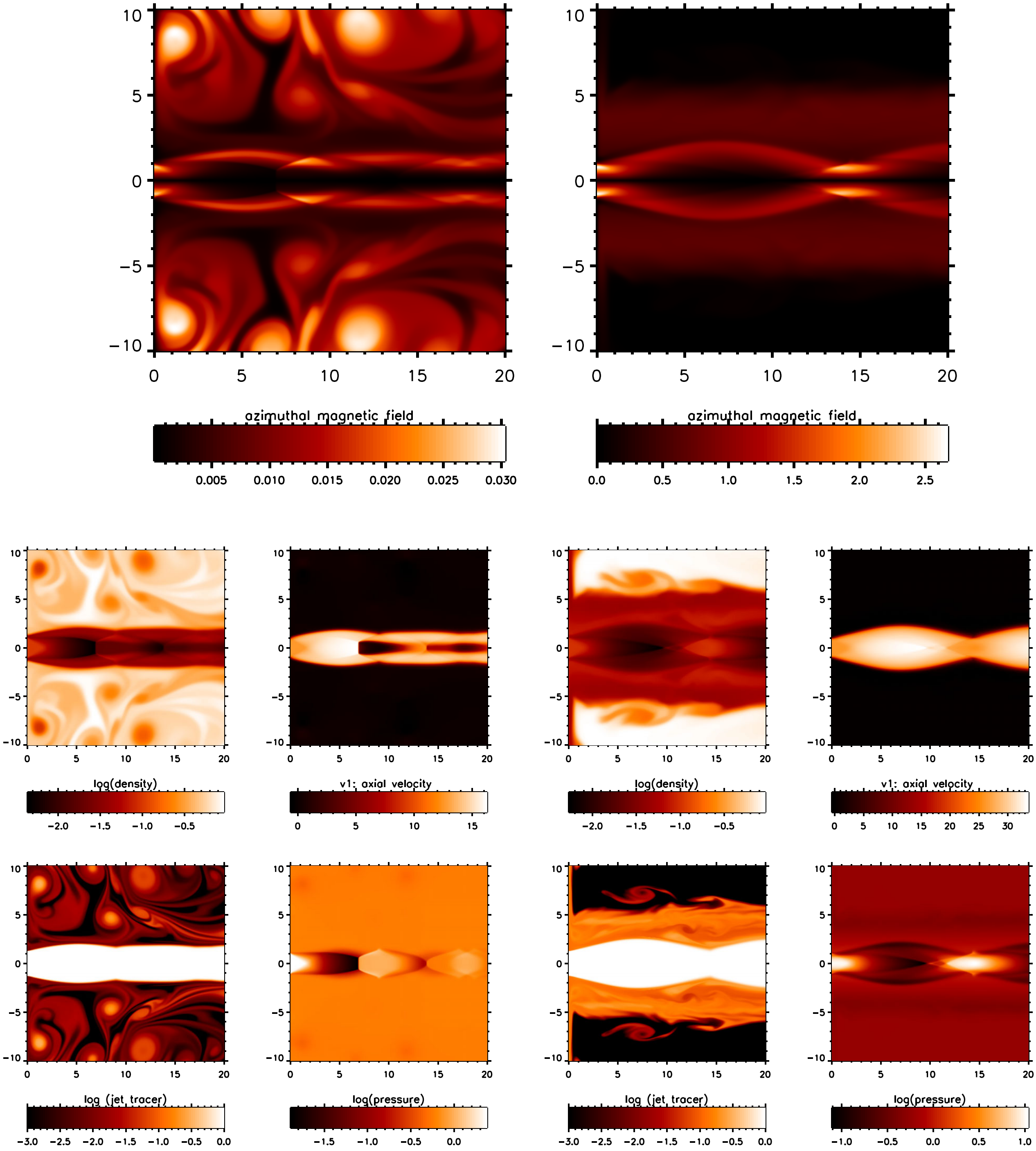

Figure 4. Passive (left) and active (right) fields at an intermediate jet overpressure. The distributions of toroidal magnetic field (top panels) and physical parameters (lower sub-panels) for $\kappa = 4$ and a passive field with $\sigma_\phi = 10^{-4}$ as well as a strong field with $\sigma_\phi = 1$. The time corresponds to the end of the simulation at $t = 200t_u$. The length scale is in units of the jet radius. Upper-left sub-panel: density, upper-right sub-panel: axial velocity, lower-left sub-panel: tracer for jet gas and lower-right sub-panel: pressure.

The shock diamonds are now less sharp and extend much further along the axis. They are thus better described as elongated or prolate structures rather than diamonds.

At high overpressures, the strong magnetic field causes a dramatic pattern change with a Mach disc being eliminated. The right-hand panels of Fig. 5 show that the jet is now highly collimated as seen in comparing the lower-left tracer sub-panels. The streamlined jet and oblique fronts negate the need for a Mach disc altogether. It is replaced by an elongated prolate structure.

To understand this change in structure, we inspect the pressure and field within the entire reservoir. Fig. 6 displays the pressure (top) and field (bottom) for both the uniform grid (left) and the

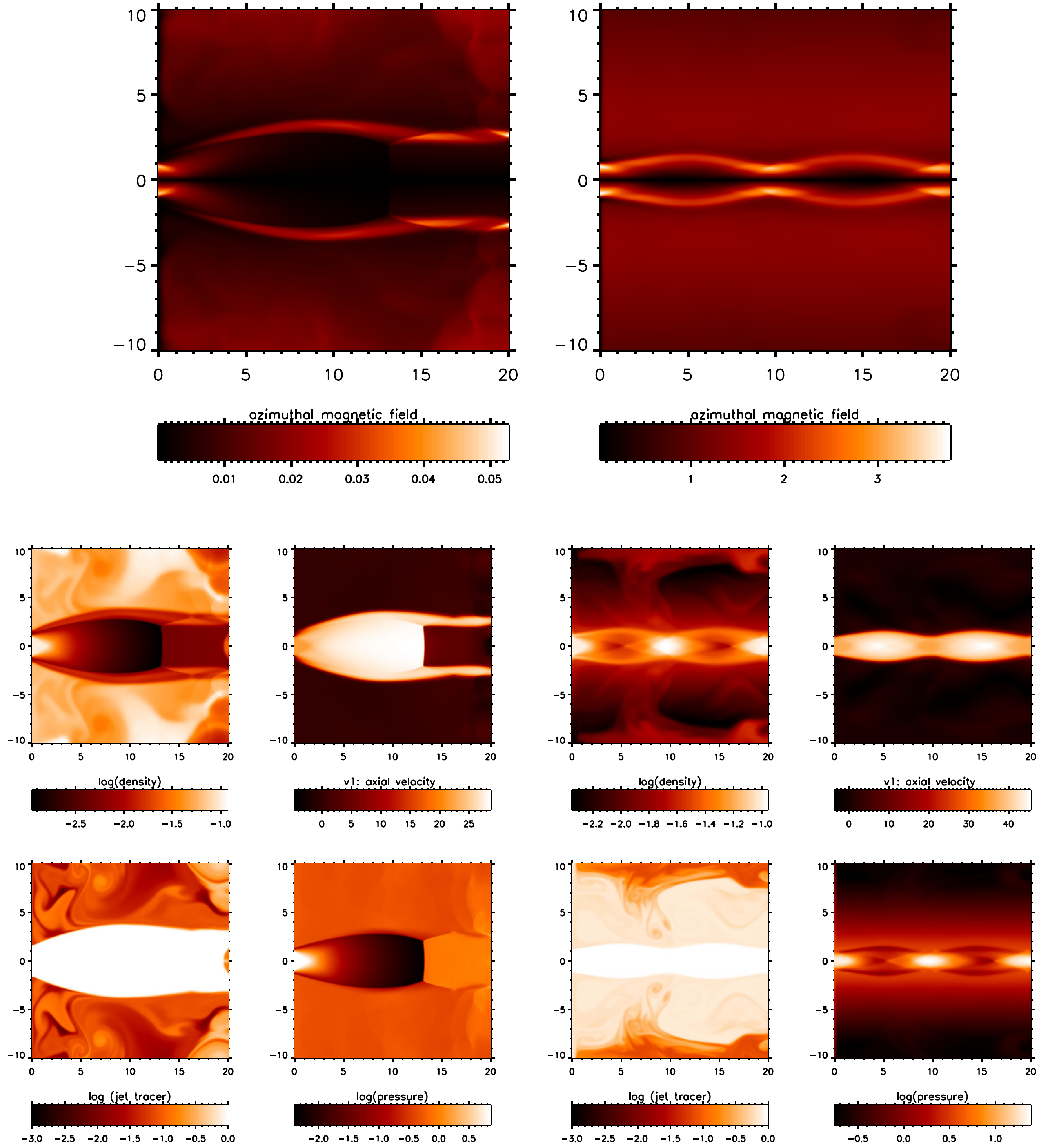

Figure 5. Passive (left) and active (right) fields at a high jet overpressure. The distributions of toroidal magnetic field (top panels) and physical parameters (lower sub-panels) for $\kappa = 8$ and a passive field with $\sigma_\phi = 10^{-4}$ as well as a strong field with $\sigma_\phi = 1$. The time corresponds to the end of the simulation at $t = 200t_u$. The length scale is in units of the jet radius. Upper-left sub-panel: density, upper-right sub-panel: axial velocity, lower-left sub-panel: tracer for jet gas and lower-right sub-panel: pressure.

entire region simulated (right) at the end of the run. Note that the ambient thermal pressure has been maintained far from the jet, a required condition for our simulations to retain their integrity. However, the jet is surrounded by a wide cocoon of ejected jet gas containing the toroidal field.

The thermal pressure is now high adjacent to the jet, but falls radially (i.e. dark blue in the top panels). The outward force is balanced by the magnetic tension in the cocoon which stretches out to $\sim 10R_{\rm jet}$. At the boundary between the cocoon and ambient medium, the thermal pressure has fallen such that the combined

Table 3. The distinct flow patterns at the end of each simulation given a range in κ and σ_ϕ. These patterns are derived using the classification outlined in fig. 2 of M. D. Smith et al. (2025). Blank entries are where no simulation was run and NA represents no distinct flow pattern.

	$\sigma_\phi = 10^{-4}$	$\sigma_\phi = 0.125$	$\sigma_\phi = 0.25$	$\sigma_\phi = 0.5$	$\sigma_\phi = 0.75$	$\sigma_\phi = 1$	$\sigma_\phi = 2$	$\sigma_\phi = 4$
$\kappa = 2$	a	a	a	b	b	b	b	b
$\kappa = 4$	d	b	b	b	b	c	b	NA
$\kappa = 6$	d	d	b	b	c	b	b	b
$\kappa = 8$	e	d	f	c	c	d	b	NA
$\kappa = 10$	f	d	f	c	c	c	b	b
$\kappa = 12$	f	f	f	e	c	c	NA	NA
$\kappa = 14$					f	c	b	d
$\kappa = 16$					f	c	NA	d
$\kappa = 18$					c	c	NA	NA
$\kappa = 20$					NA	c	NA	b

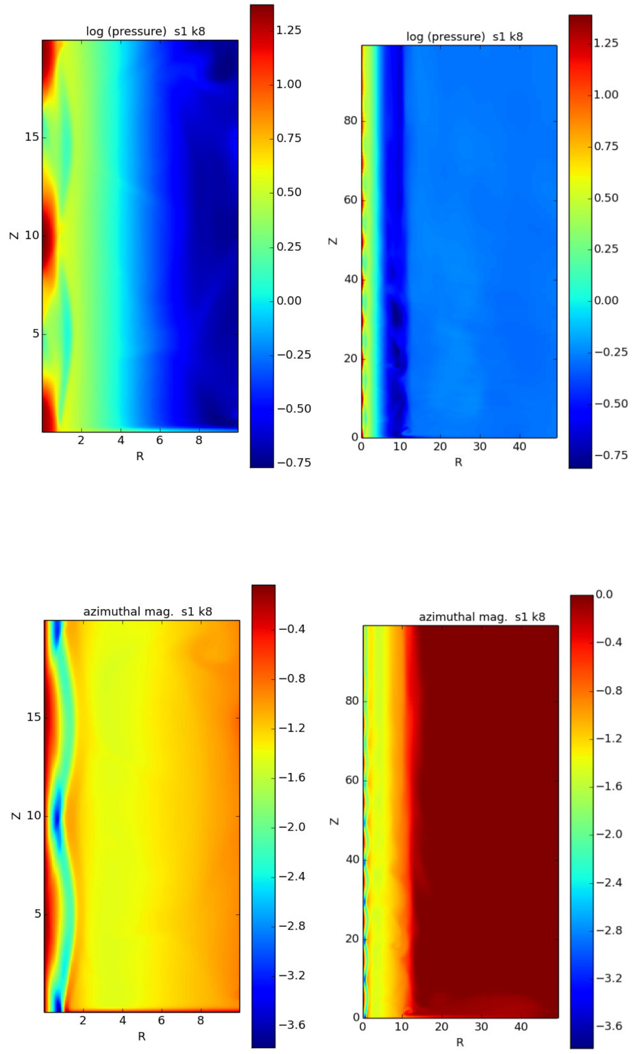

Figure 6. Pressure and magnetic field distributions. The distributions of pressure (upper) and toroidal magnetic field (lower panels) across the uniform grid section (left) and the entire simulated domain (right panels). This is for $\sigma_\phi = 1$, $\kappa = 8$ and at time $t = 200t_u$ which is the end of the simulation.

thermal and magnetic pressures balance the ambient thermal pressure. Hence, the development of the cocoon of jet overspilled gas reduces the effective overpressure on the jet itself, ultimately due to the magnetic tension in the cocoon.

The cocoon's low density yet high pressure means this gas is hot. It is sufficient to inhibit the diverging jet by raising the thermal pressure from the original value of 0.6 to ~ 3. Thus it is the raised ambient pressure which reduces the overpressure to a level where regular reflection is sufficient.

A Mach disc could be present instead within an alternative scenario. If the ambient medium is a slow wind which encompasses the jet, this blows the adjacent gas clean of jet overflow gas (Jyothy et al., 2026). We suspect that the result is a flow pattern similar to the passive field case.

At the intermediate overpressure, illustrated in Fig. 4, the spine-sheath structure is not present when the field is strong. A cocoon still enshrouds the jet but the jet diverges as it exits. In such a case, the flow structure can be prone to oscillations which increase the pressure adjacent to the jet. However, these oscillations are completely suppressed by the magnetic field (see below).

In summary, the effects of the field are as follows: at low overpressures we note that the jet diverges more as it exits. It then remains wider and converges further downstream. For high overpressures, the jet has generated a cocoon of sufficient pressure to counteract the overpressure and so better collimating the jet. Thus much depends on how the jet is set up and the maintenance of an encompassing cocoon in that process.

4.3 Time-dependent behaviour

To analyse the time-dependent properties, we can explore movies and space-time diagrams. The latter displays a physical parameter of a 1D distribution as a function of time. The pressure distribution along the jet axis is taken as the x-coordinate while the vertical axis shows how this distribution changes with time. In particular, the distance between the nozzle and the stand-off shock is a defining measure of variability.

To this point, the general characteristics have been analysed through inspection of the cross-sectional snapshots of pressure. However, steady shock configurations are not the rule at high overpressures even in the absence of the magnetic field. A feedback loop between the jet and ambient medium supports oscillations that send sound waves laterally, generating the

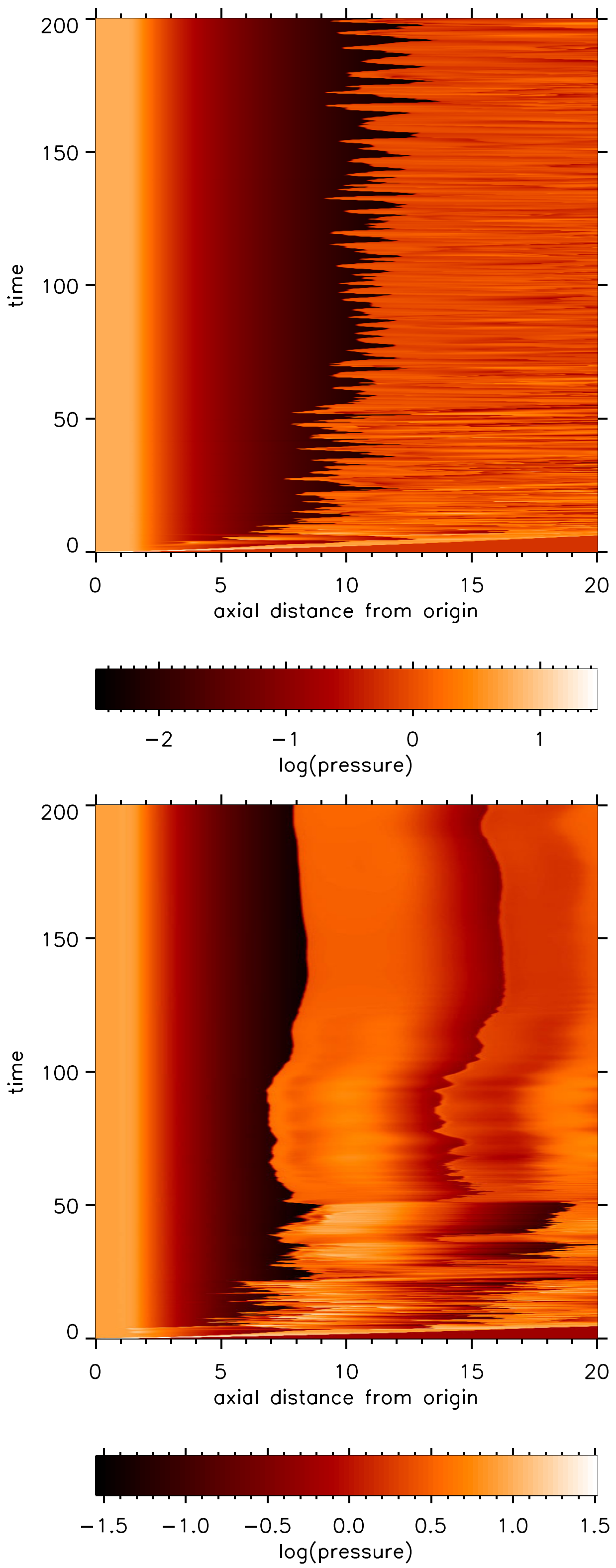

Figure 7. Space-time diagrams for jets with a strong magnetic field with $\kappa = 10$. The upper panel corresponds to $\sigma_\phi = 10^{-4}$ and the lower panel to $\sigma_\phi = 0.125$. The distribution of the pressure along the jet axis (x-axis) is shown as a function of the time (y-axis). Length scale is in units of the jet radius.

well-known noise or high-pitched screeching from exhausts. A passive field yields results consistent with the absence of a field. Quasi-stationary shock configurations are found for $\kappa < 4$ although small amplitude oscillations are discernable. However, for high κ, large rapid oscillations occur as shown in the top panel of Fig. 7.

Remarkably, even a low magnetic field is sufficient to suppress the oscillatory spikes after an initial period of adaption. The lower panel of Fig. 7 demonstrates this for $\sigma_\phi = 0.125$ where we take the same κ value as in the passive case of the upper panel. Note that regular reflection occurs even with this weak field, as evidenced by the second distinct shock appearing at $\sim 16R_{\rm jet}$ following the stand-off at $\sim 8R_{\rm jet}$. The suppression of high-frequency oscillations continues as higher toroidal magnetic fields are applied.

However, a new low-frequency mode appears as per Fig. 8 where the toroidal field is dominant. This mode has high amplitudes and affects all high κ simulations and dominates for $\kappa = 6$ and above for $\sigma_\phi = 1$.

We find these high-frequency oscillations to arise for all $\kappa > 4$ for a passive toroidal field (e.g. the upper panel of Fig. 7). However, with $\sigma_\phi \geq 0.125$, high-frequency noise is only present during the initial jet settling phases (e.g. the lower panel of Fig. 7).

Major low-frequency oscillations occur in the jet cocoon that feed back on to the jet. The result is that the location of the stand-off shock in the jet is subject to large variations (see Fig. 8). We find that these large amplitude variations only occur for $\sigma_\phi \geq 0.5$ and $\kappa \geq 6$ for both $\sigma_\phi = 0.5$ and $\sigma_\phi = 0.75$. It occurs at lower κ for $\sigma_\phi \geq 1.0$ and $\kappa = 2$ for $\sigma_\phi = 4$.

A cocoon around the jet was first noted by M. L. Norman et al. (1982) in 2D HD simulations. For a light jet, there is a fast back-flow in the cocoon due to the strong shock heating and ram pressure at the working surface. The flow into the cocoon is accelerated. Moreover, the back-flow is dominated by oscillations of the working surface which feed vortices into the cocoon generating large-scale waves in the cocoon (M. D. Smith et al. 1985; K. R. Lind et al. 1989). The vortex shedding from the working surface will be amplified in the present case due to the diverging-converging nature of the overpressured jet.

At very early times, the thermal pressure in the cocoon is high and self-similar solutions for the jet evolution are attainable. After this early phase, the cocoon expands so that pressure equilibrium with the ambient medium is maintained. In the MHD case however, the magnetic tension in the cocoon alters the effective jet overpressure. This not only alters the flow pattern but also introduces large oscillations.

4.4 Stand-off distance

The stand-off distance is a significant diagnostic in the analysis of observations, simulations and laboratory experiments. Consistent with previous works, we take the stand-off shock distance, d, as the distance from the nozzle to the first rise in pressure along the axis.

The distance d increases with κ as shown in the top-right panel of Fig. 9 for the passive field. This is in keeping with the HD case where we confirmed in SK22 that the stand-off distance of the regular reflection is $\propto \kappa$ and for Mach discs is $\propto \sqrt{\kappa}$.

For a passive field, we find that the position of the stand-off shock varies stochastically for $\kappa > 6$ with a short time-scale of up to $(2–5)t_u$. In this regime, pressure disturbances occur in the jet which feed back into the ambient medium. In turn, the ambient

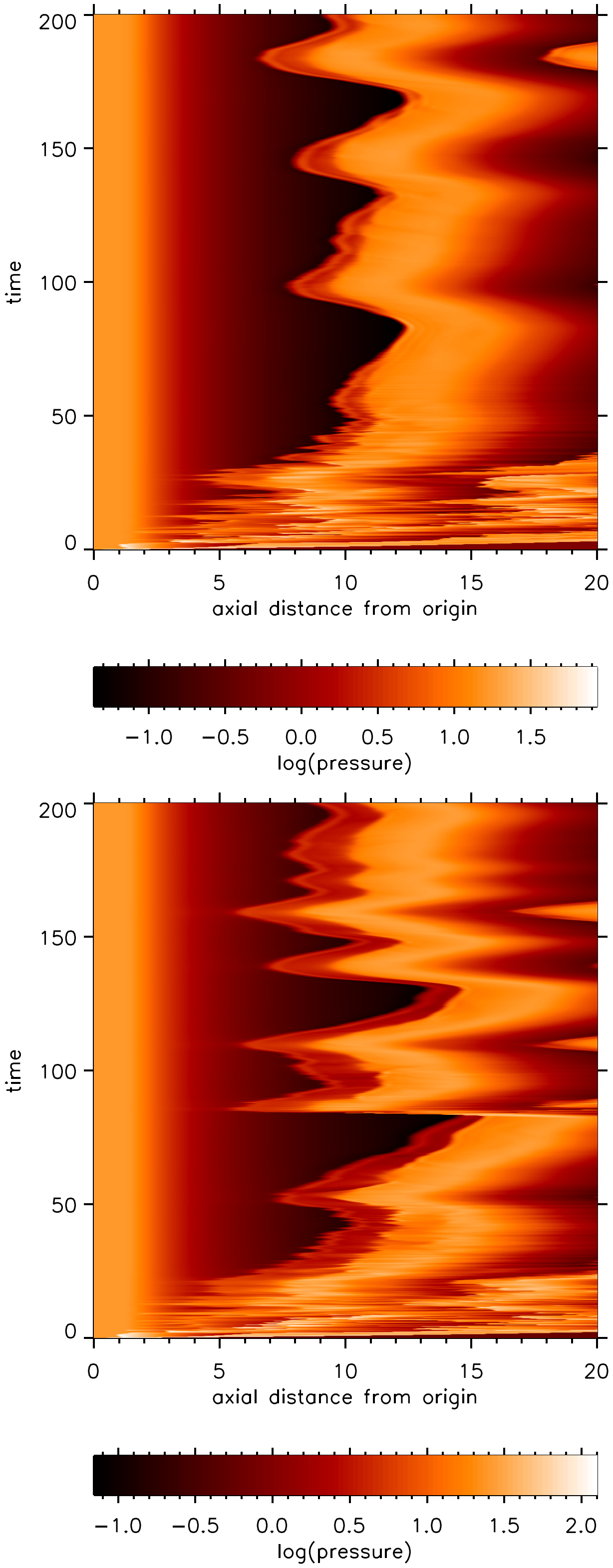

Figure 8. Space–time diagrams for jets with a strong magnetic field with $\kappa = 10$. The upper panel corresponds to $\sigma_\phi = 0.5$ and the lower panel to $\sigma_\phi = 1$. The distribution of the pressure along the jet axis (x-axis) is shown as a function of the time (y-axis). Length scale is in units of the jet radius.

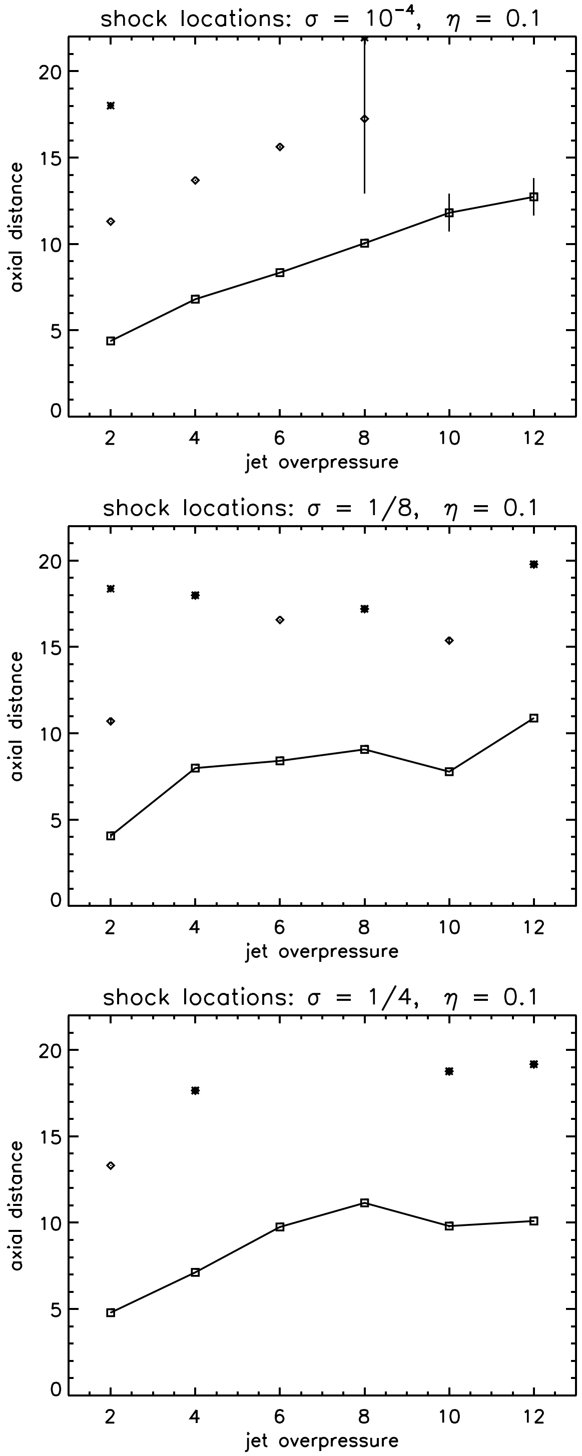

Figure 9. **Stand-off distance of the first shock for weak fields.** The shock front distances, d, of the shocks along the jet axis as a function of the simulation overpressure, κ, in units of the jet radius. Upper panel: the passive field, middle panel: $\sigma_\phi = 0.125$ and lower panel: $\sigma_\phi = 0.25$. This is our standard set up with $M_{\rm jet} = 2.0$ and $\eta = 0.1$. The stand-off shock locations are designated with square symbols and the outer shocks, where found, with diamonds.

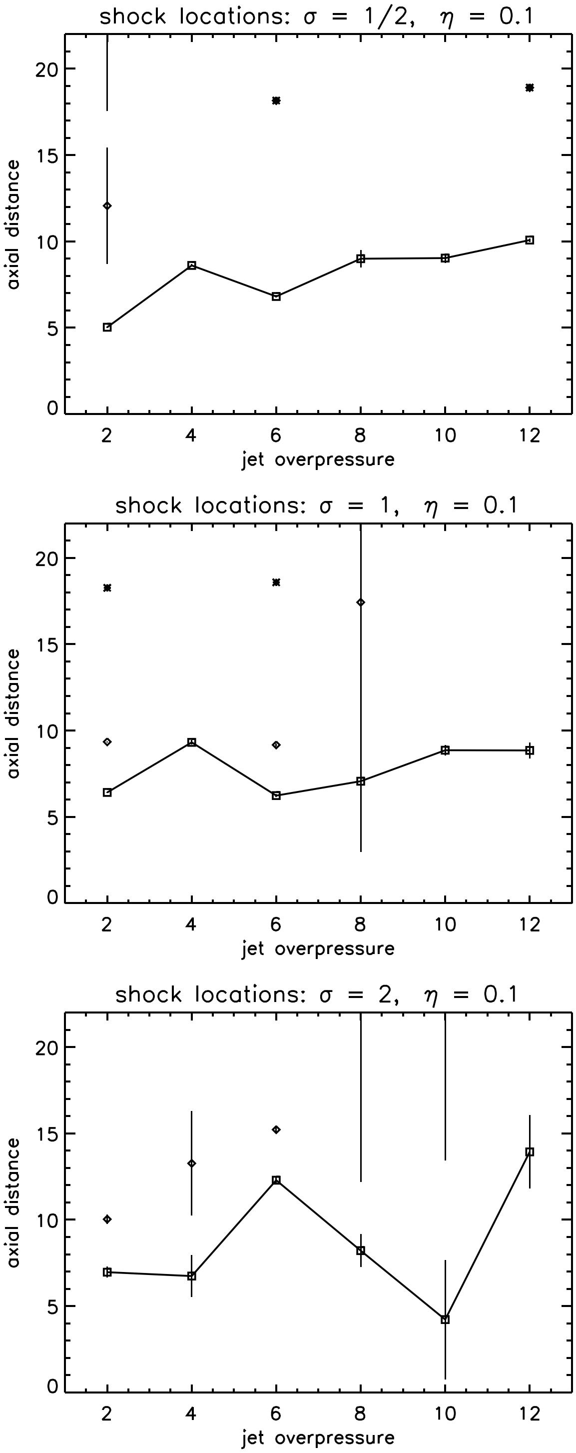

Figure 10. Stand-off distance of the first shock for strong fields. The shock front distances, *d*, of the shocks along the jet axis as a function of the simulation overpressure, κ, in units of the jet radius. Upper panel: $\sigma_\phi = 0.5$, middle panel: $\sigma_\phi = 1$ and lower panel: $\sigma_\phi = 2$. This is for our standard set up with $M_{\rm jet} = 2.0$ and $\eta = 0.1$. The stand-off shock locations are designated with square symbols and the outer shocks, where found, with diamonds.

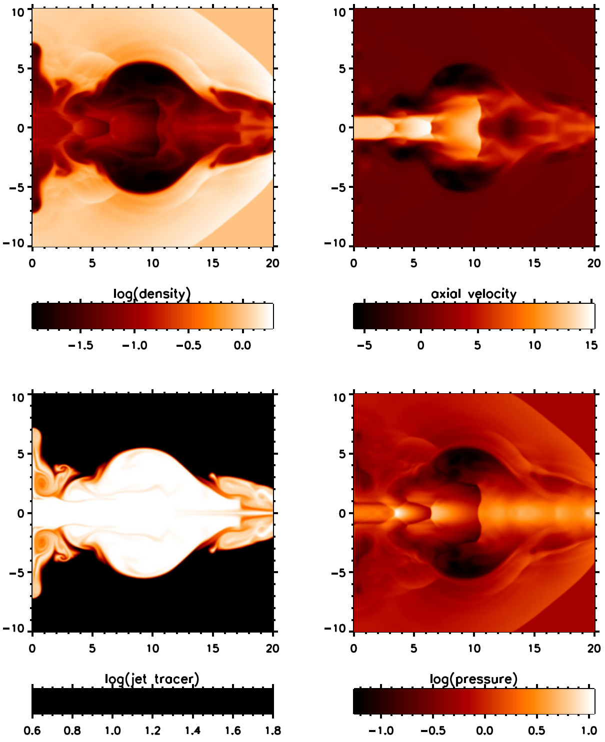

Figure 11. Early nose cone development. The production of a nose cone in the initial advancement onto the grid by showing the distributions of physical parameters for $\kappa = 1$ and a strong field with $\sigma_\phi = 1$. The time corresponds to $t = 8t_u$. The length scale is in units of the jet radius. Upper-left sub-panel: density, upper-right sub-panel: axial velocity, lower-left sub-panel: tracer for jet gas and lower-right sub-panel: pressure.

medium transmits the pressure variations upstream (C. K. W. Tam 1995). This alters the overpressure and the stand-off shock location adjusts, completing the hysteresis loop. It should be remarked that the transition between flow patterns is not fixed and the variations can lead to Mach discs temporarily appearing or disappearing as the shock position moves. Here, we superimpose vertical bars which represent root-mean-square deviations in *d* over the final $2t_u$.

The stand-off distance remains in the range $\sim (4\text{–}12)R_{\rm jet}$ despite the wide ranges in κ and σ_ϕ. The effect of high overpressures appears to be largely offset by the associated magnetic tension in the adjacent cocoon.

5 PRESSURE-MATCHED AND OVERDENSE JETS

The means to distinguish between pressure-matched jets and overpressured jets is established below.

Pressure-matched jets with strong toroidal fields have long been known to promptly develop nose cones (K. R. Lind et al. 1989). A nose cone is a high pressure cylindrical extension along the jet axis, formed of a portion of the shocked gas which is not ejected radially. This is also reproduced here in Fig. 11, where we take $\kappa = 1$ and $\sigma_\phi = 1$. The nose cone is generated as a result of the tension in the toroidal field generating a force towards the jet axis. The nose cone is prominent in the pressure distribution as shown in Fig. 11.

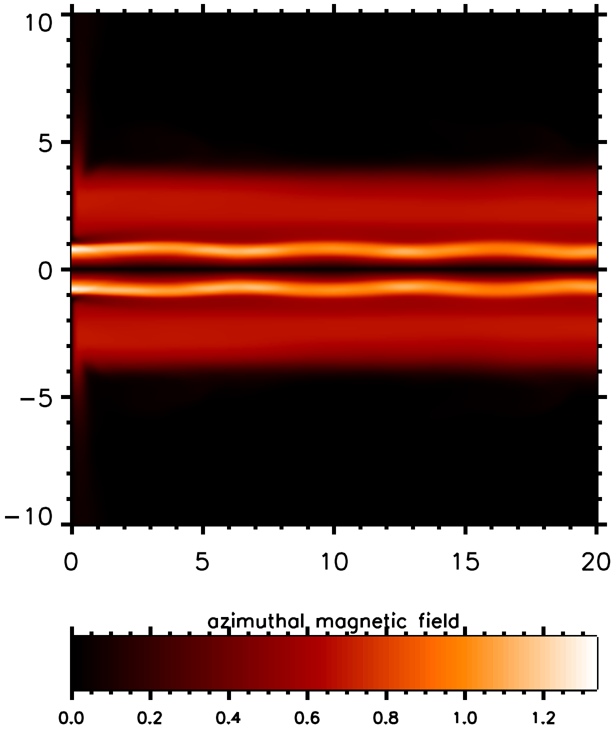

Figure 12. The smooth final toroidal field distribution in a pressure-matched jet. The distribution of toroidal magnetic field for $\kappa = 1$ and a strong field with $\sigma_\phi = 1$. The time corresponds to the end of the simulation at $t = 200 t_u$. The length scale is in units of the jet radius.

However, a radial expulsion of gas into the cocoon still prevails. The upper-right panel of Fig. 11 elucidates the complex dynamics: the entire nose cone is indeed moving forward but the wide cocoon of back-flowing gas stems from the termination shock.

Similarly even with our equilibrium jets in which thermal pressure provides a counter-balancing force, nose cones develop. Moreover, the overpressure does not alter this flow pattern as can be seen in the movies. However, the nose cones are only present in the initial advancement which has been simulated to times of up to $10 t_u$ in previous simulations. In our present set of simulations, we find that nose cones do indeed develop for $\sigma_\phi = 1$ at all overpressures during the initial advance on to the uniform grid which we display in Fig. 11. The nose cone is evident in the pressure and axial velocity snapshots. On the other hand the back-flow is clearly developing with a high negative speed, filling out a bloated cocoon.

Given sufficient time, the pressure-matched jet settles down into a steady state in the nozzle near-field. Going to $200 t_\mathrm{u}$, we find that the cocoon has developed around the jet and a back-flow carries a smooth toroidal field with it, as well illustrated in Fig. 12.

The equilibrium reached is elucidated in Fig. 13 in which radial profiles along the nozzle entry plane are shown. Internal to the jet, the thermal pressure gradient balances inward magnetic forces. In particular, a strong magnetic pressure gradient is present. In the cocoon, however, which is a mixture of hot ambient material and shocked jet gas, the toroidal field tension and thermal pressure gradient combine to create a smooth steady shroud to the jet. The magnetic field itself is relatively constant in the cocoon whereas the thermal pressure rises above the reservoir value of 0.6 to a value of 1.0 at the inner interface with the jet, balancing the magnetic tension force.

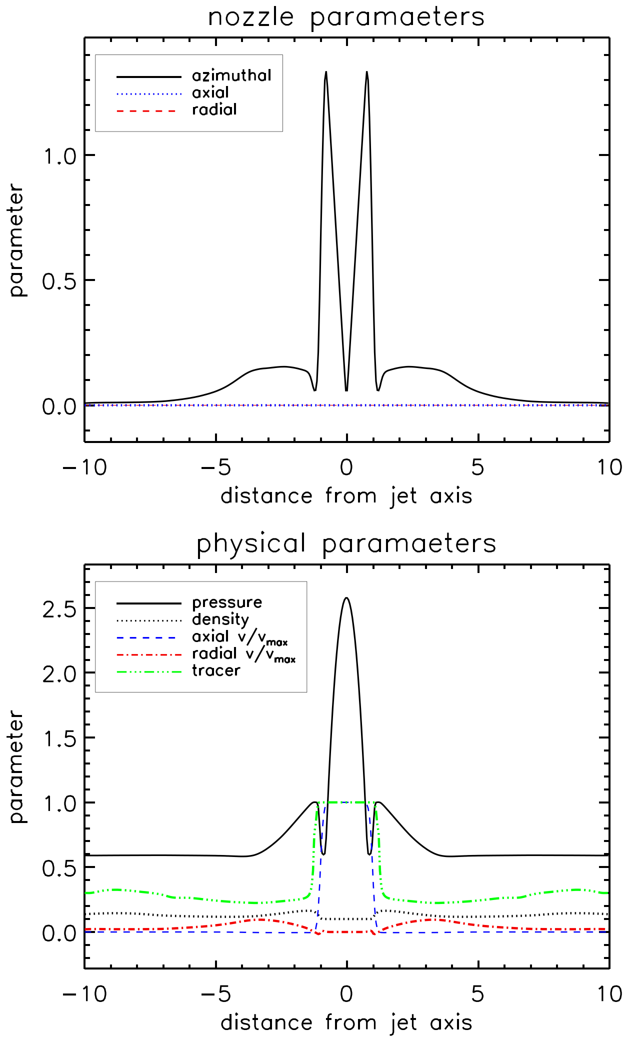

Figure 13. Inflow boundary: pressure-matched jet. The physical and magnetic field parameters across the inflow boundary at the end of the simulation with a time of $t = 200 t_u$ for $\sigma_\phi = 1$ and $\kappa = 1$. The velocities are normalized to the maximum velocity of $v_\mathrm{max} = 13.112$ to 3dp for ease of display.

In summary, high-amplitude low-frequency oscillations are a feature of overpressured jets with high magnetic fields but are absent from pressure-matched jets. They are caused by variations in feedback through the jet overspill into a back-flowing cocoon which is triggered by the jet's reaction to the overpressure.

Cocoons do not accompany dense jets and so we expect them not to be prone to the long-period instability. To confirm the above analysis, we simulate a high density jet with $\eta = 10.0$. In this case, we expect no cocoon to develop since the gas which spills over from the rapidly advancing working surface does not flow back (SK22). This is borne out as seen in Fig. 14 which shows that there is no significant cocoon for $\sigma_\phi = 1$. Moreover, a Mach disc is present. Thus the flow pattern changing due to the strong toroidal field is almost entirely attributable to the presence of a cocoon rather than internal effects within the jet.

Space–time diagrams for the simulations analysed in this section are provided in Fig. 15 and show the stability of these jets

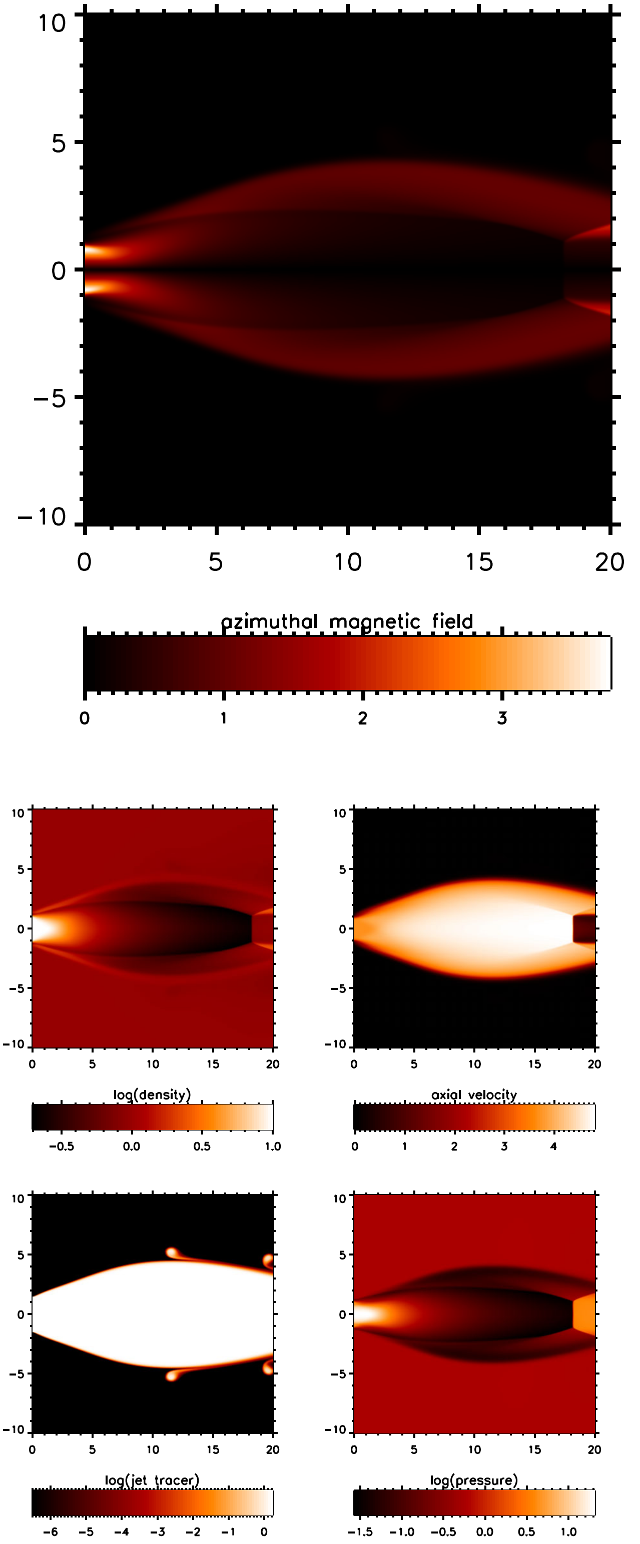

Figure 14. High density and strong toroidal field. The distributions of toroidal magnetic field (top panel) and physical parameters (lower sub-panels) for a jet with a relative density of $\eta = 10$, $\kappa = 8$ and a strong field with $\sigma_\phi = 1$. The time corresponds to the end of the simulation at $t = 200 t_u$. The length scale is in units of the jet radius. Upper-left sub-panel: density, upper-right sub-panel: axial velocity, lower-left sub-panel: tracer for jet gas and lower-right sub-panel: pressure.

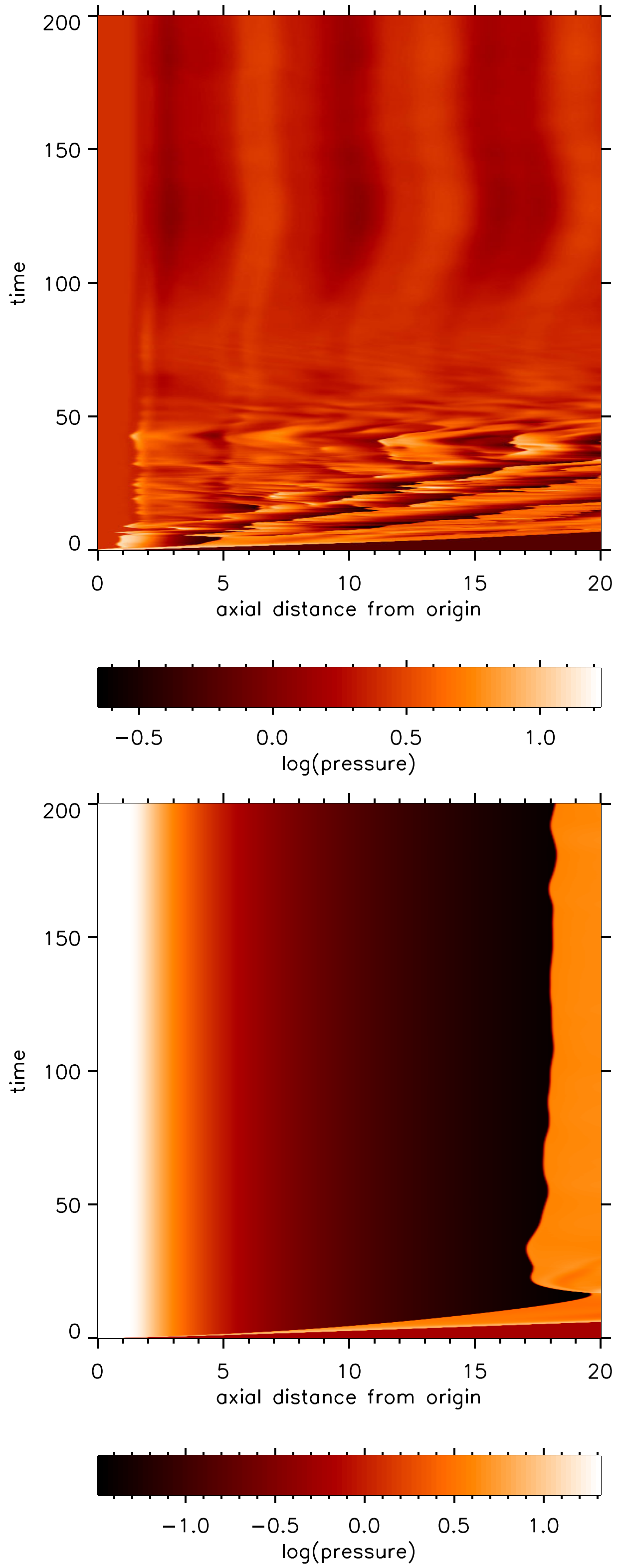

Figure 15. Space–time diagrams for jets with a strong magnetic field with $\kappa = 1$, $\eta = 0.1$ (upper panel) and $\kappa = 8$, $\eta = 10$ (lower panel) corresponding to $\sigma_\phi = 1$. The distribution of the pressure along the jet axis (x-axis) is shown as a function of the time (y-axis). Length scale is in units of the jet radius.

in the near-field. The upper panel demonstrates that the shock pattern disappears once the turbulence in the cocoon has decayed after $t_{\rm u} \sim 50$. The lower panel shows that the absence of a cocoon to enshroud a high density jet leads to a steady flow pattern. Hence, a strong magnetic field in a high high-density jet stabilizes a Mach disc.

6 DISCUSSION

6.1 Main results

The following results apply to the near-field of overpressured jets well after the constant outflow from a circular nozzle has penetrated far beyond a giant reservoir surrounding the region of interest. By holding the axial Mach number constant, we are able to reveal the full set of flow patterns for entire ranges of overpressure and magnetic field:

(i) Simulations with a near-passive magnetic field confirm that the flow patterns and shock configurations are identical to those found with the purely HD version of the PLUTO code by SK22.

(ii) However, remarkably the field is strongest within large vortices occupying the cocoon adjacent to the jet. These field-dominated vortices are reflected in the jet tracer distributions which correspond to hot, low density gas spilled over from the advancing jet.

(iii) The field within the jet itself traces that imposed at the nozzle with small oblique arc-shaped field enhancements within a sheath. Thus the strong pressure jumps at Mach discs for high overpressures, or at shock diamonds for low overpressures, are not significantly altered when a weak field is present.

(iv) A strong toroidal field converts shock diamonds into filled elongated high-pressure prolate features. The tension of the surrounding jet magnetic field is high at the widest point of the prolate minor axes.

(v) A strong toroidal field does not eliminate Mach discs which still arise for combinations of high overpressures and moderate magnetic fields.

(vi) Exploring the entire chain of shocks in the near-field of the nozzle, we find that all six shock chain configurations identified by M. D. Smith et al. (2025) are found in the σ_ϕ–κ phase space.

(vii) The distance to the stand-off shock increases with the overpressure for low σ_ϕ but does not significantly depend on either the overpressure or the relative field strength at high overpressures.

(viii) High-frequency oscillations generate exhaust noise within gas jets. Here, we find that the toroidal field suppresses these oscillations. Instead, a low-frequency high-amplitude oscillation occurs with a strong field provided the diverging-converging jet has pumped gas into a cocoon. This pump sets up a cocoon in which magnetic tension is balanced by a negative radial pressure gradient.

(ix) It is thus concluded that a cocoon is responsible for moderating the shock configuration and causing the large oscillations in the overpressured jet.

(x) The density ratio effects the high-frequency noise but not the flow pattern. However, a heavy jet does not form a backflow within a cocoon and the long period variations are absent. A cocoon also does not occur in other scenarios. For example, a surrounding co-axial wind can blow the cocoon away as found in the HD case.

The distinctive signature of strong toroidal fields is the chain of elongated pressure features. Observationally, it is tempting to associate these to knots in radio galaxy and protostellar jets which display elongation (e.g. V. Velović et al. 2022). However, this requires further analysis which we undertake in a following work. We note here that the strong field lies external to the knots of shocked gas where particle acceleration may boost the relativistic electron population in the spine.

Non-thermal emission from jets driven by massive stars are attributable to synchrotron radiation (W. O. Obonyo et al. 2019). In the present model context, we suggest that a field component would provide a more plausible means of generating synchrotron from the shocks which dominate close to the jet spine (e.g. A. Fuentes et al. 2021). This will be explored in a companion study. We can also consider whether the magnetized cocoon can generate a diffuse synchrotron cloak around a jet.

The important effect of a variable cocoon on overpressured jets has been previously brought to our attention by F. Rubini et al. (2007). They simulated axisymmetric HD jets with radiative cooling. In the early stages, the stationary shock pattern is set up. However, the surrounding cocoon loses pressure through cooling. The inner shocks then move out due to the increased overpressure giving rise to proper motions. The proper motions thus found are exclusively away from the source but are limited to speeds far below the jet speed. Dependent on the change in shape of the channel, the shock positions are not given by the jet dynamical time but the appropriate Kelvin–Helmholtz time-scale as defined by the surface wave speed and the displacement of the stand-off shock (SK22). In the present MHD simulations without cocoon cooling, the changes in the jet shock configuration are both away and towards the jet source, as well as very slow, as illustrated in the space–time diagrams. Note that high sustained proper motions are feasible in overpressured jets by invoking a long-term restarting jet (F. Rubini et al. 2007) or prolonged bursts (Richards & Smith, 2026).

6.2 Power diagrams: the transport of energy

The question of dynamical feedback from within a galactic nucleus or protostellar core through an outflow has been posed (e.g. J. Silk & M. J. Rees 1998; C. J. Davis et al. 2007). In the present context, we can calculate the flux of energy transmitted into the environment. To do so, we determine the integrated power through the girth and cap of a cylindrical surface situated at 90 per cent of the radial and axial distance displayed in the above figures as a function of time. The initial advance of the bow shock is rapid as evident in the top panel of Fig. 16 where the power lateral to the jet rises after just a few tine units (black dash–dotted line) and it takes only $20t_{\rm u}$ to cross the grid (red dashed line).

With a passive field, there are two cases of interest. At low overpressures, once a jet has advanced beyond the near field a steady jet has minimal effect on the adjacent surroundings (see the top panel of Fig. 16). On the other hand, the high-frequency exhaust noise associated with higher overpressures transmits a significant flux laterally, as illustrated in the lower panel of Fig. 16.

In the active field case, the high-frequency noise is absent. Instead, with a sufficient overpressure, the large-amplitude low-frequency modes take over. As shown in Fig. 17 (top panel), these cause dips in the total power exiting the grid. The dips correspond to spikes in the lateral energy flow as shown in the lower panel

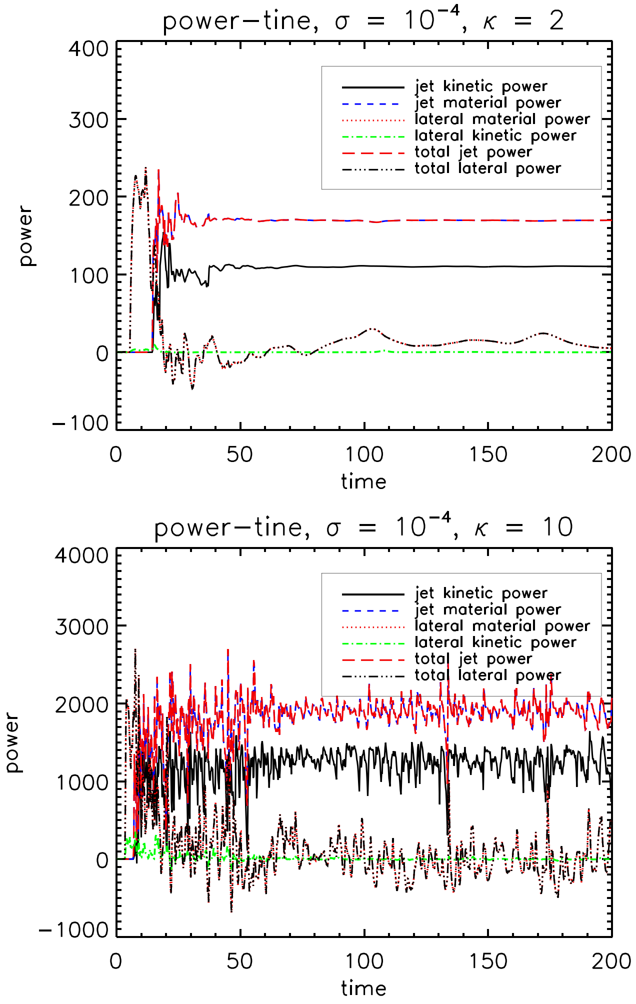

Figure 16. Evolution of the lateral and forward escape of energy for a passive field, $\sigma_\phi = 10^{-4}$, with overpressures $\kappa = 2$ (upper panel) and $\kappa = 10$ (lower panel) for light jets ($\eta = 0.1$). The energy flux is out of a cylindrical surface drawn with radius 180 zones and axial length 710 zones. Initially, the jet enters the grid and it takes $\sim 30t_u$ to cross to the cylinder cap which is at 90 per cent of the uniform grid length. The power is expressed in simulation units of $\rho_{\rm amb}c_{\rm amb}^3R_{\rm jet}^2$.

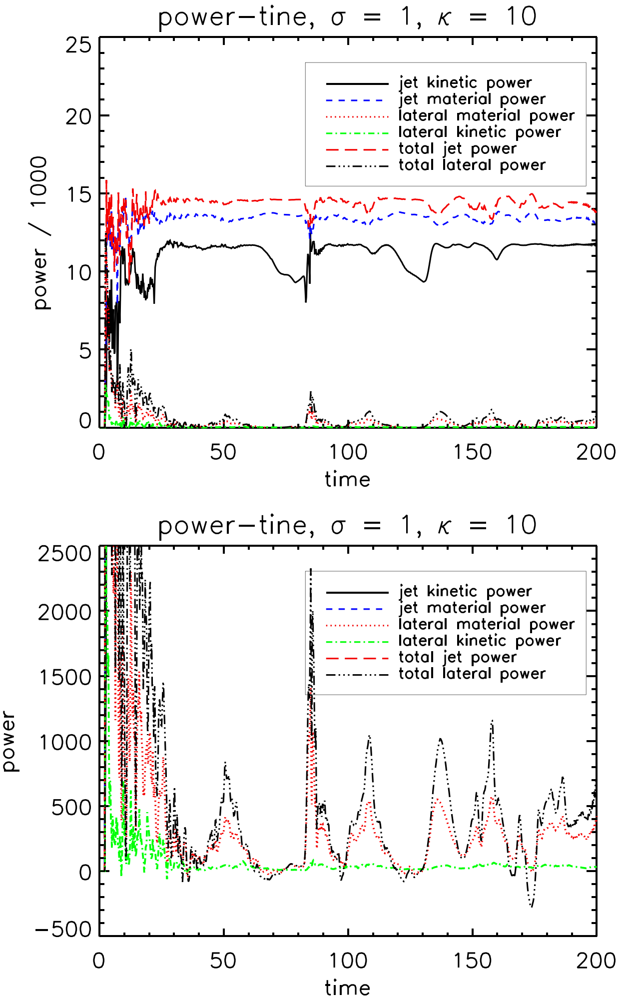

Figure 17. Evolution of the lateral and forward escape of energy for an active field, $\sigma_\phi = 1$, with overpressures $\kappa = 10$ showing all the powers (upper panel) and zooming in (lower panel) for light jets ($\eta = 0.1$). The energy flux is out of a cylindrical surface drawn with radius 180 zones and axial length 710 zones. Initially, the jet enters the grid and it takes $\sim 30t_u$ to cross to the cylinder cap which is at 90 per cent of the uniform grid length. The power is expressed in simulation units of $\rho_{\rm amb}c_{\rm amb}^3R_{\rm jet}^2$.

of Fig. 17 which zooms in on the lower power range. The lateral power can reach values of up to ~ 8 per cent of the jet power for 10 per cent of the time. This is a means to transmit ripples of well-spaced energy waves that deserve further attention in terms of observational signatures although the long-term influence on the energy budget of the ambient medium would be minimal.

Thus the cocoon back-flow triggers long-term jet variability. While the field damps all the high-frequency noise, the cocoon-triggered motions can be seen to affect the radial energy flux While high-frequency oscillations occur for $\kappa = 8$ and above. Even a weak field damps the high-pitched noise in the case studied here up to $\kappa = 12$.

However, the noise is not replaced by the low-frequency modes. These modes are absent in our weak-field cases, $\sigma_\phi = 1/4$ and below, for all the overpressures covered here, $\kappa \le 12$, and begin for overpressures in excess of the following critical values:

$\sigma_\phi = 1/2$ for $\kappa \geq 8$,
$\sigma_\phi = 3/4$ for $\kappa \geq 6$,
and
$\sigma_\phi = 1$ for $\kappa \geq 4$.

We should also expect kinetic energy to be dissipated across the interface between the supersonic jet flow and the cocoon where a high-velocity gradient occurs. The growth of surface instabilities, in the form of Kelvin–Helmholtz pinch, helical and fluting modes, have been investigated in the MHD context (A. Ferrari, S. Massaglia & E. Trussoni 1982). The fastest growing are 2D reflection modes while 3D modes become significant further downstream. Hence, we can assume here that surface instabilities do not affect the region in proximity to the nozzle. Heating, particle acceleration and magnetic field amplification take place across the boundary shear layer where kinetic energy is dissipated (E. P. Alves et al. 2014; J.-S. Wang et al. 2023). In the present case, in the absence of a radial magnetic field and narrow shear layer, the inviscid flow is globally valid.

7 CONCLUSIONS

We have performed prolonged jet simulations in order to ascertain the final state of evolution of an overpressured MHD jet with a toroidal magnetic field. The set-up is crucial to the resulting properties and needs to be clearly expressed.

The jet enters from a circular nozzle and maintains axial symmetry. The gasses are adiabatic and the initial ambient medium is an extremely large uniform reservoir in order to avoid any numerical boundary effects. In addition, the injected jet is in radial force balance such that no internal shocks or pinching occurs when the jet is not overpressured. This requires a high jet pressure along the axis to counter magnetic tension. We may thus explore the properties purely due to two parameters: the degree of overpressure and the relative field strength.

Previous work exploring this scenario was able to generate the nose cone and a back-flowing cocoon D. Kossl, E. Muller & W. Hillebrandt (1990) for a light (underdense) jet. This is reproduced here as shown in Fig. 11. However, allowing for a prolonged development, the back-flow becomes prominent. The varying cocoon pressure associated with this back-flow causes the diverging-converging jet shape to experience oscillations. This manifests itself in both the locations of the shocks and the strong bursts of energy into the ambient medium. The variation timescale is $(20 - 50)t_\mathrm{u}$.

Among the many results listed in Section 6.1, perhaps the most significant theoretically is the division of flow patterns into three regimes. Steady flow patterns involving a chain of high-pressure knots are associated with low overpressures and weak fields. High-frequency oscillations are associated with Mach discs at high overpressures.

Strong fields generate chains of prolate high-pressure knots. Large-amplitude long-period variations appear superimposed when a significant overpressure above a critical value is present. This critical overpressure is reduced as the field strength increases.

Observationally, the main result is the change in shape of the jet knots from diamonds to long pointed lenses. The long period variations may possess identifiable characteristics within simulated spectroscopic or snapshot images. Simulated images are now planned. We note here the lack of Mach discs when the toroidal field is strong. We also expect synchrotron distributions to contrast with those where the emissivity depends only on the thermal state and thus radio jets originating from AGN and protostars would be fundamentally different. In this respect, it is essential to perform a similar study with the inclusion of a poloidal magnetic field.

We note the limitations of the present study. Axisymmetric simulations do not allow for disturbances to the circular nozzle cross-section or for general inhomogeneities in the ambient medium. Symmetry can be broken by a number of processes including surface instabilities. Helical or kink instabilities may not be significant in the near-field to the nozzle but would be promoted if a small jet wiggle or precession would be superimposed. This is now being studied by us in terms of overpressured jets. This research will require 3D RMHD simulations to confirm the contents in this report.

DATA AVAILABILITY

No new observational data was generated or analysed in support of this research. Simulation source files are available on request. The data underlying this article will be shared on reasonable request to the corresponding author.

Underlying 1000-frame movies of a selection of simulations are available on the Zenodo repository at https://zenodo.org/records/19047891 or DOI 10.5281/zenodo.19047891.

REFERENCES

Alves E. P., Grismayer T., Fonseca R. A., Silva L. O., 2014, New J. Phys., 16, 035007
Arshakian T. G., Hambardzumyan L. A., Pushkarev A. B., Homan D. C., 2024, A&A, 692, A127
Bonito R., Orlando S., Miceli M., Peres G., Micela G., Favata F., 2011, ApJ, 737, 54
Cerutti B., Giacinti G., 2023, A&A, 676, A23
Chou Y.-R. et al., 2025, ApJ, 983, 6
Clarke D. A., Norman M. L., Burns J. O., 1986, ApJ, 311, L63
Cohen M. H. et al., 2015, ApJ, 803, 3
Davelaar J., Philippov A. A., Bromberg O., Singh C. B., 2020, ApJ, 896, L31
Davis C. J., Kumar M. S. N., Sandell G., Froebrich D., Smith M. D., Currie M. J., 2007, MNRAS, 374, 29
Ferrari A., Massaglia S., Trussoni E., 1982, MNRAS, 198, 1065
Franquet E., Perrier V., Gibout S., Bruel P., 2015, Progr. Aerospace Sci., 77, 25
Fu W., Liang E. P., Tzeferacos P., Lamb D. Q., 2015, High Energy Density Phys., 17, 42
Fuentes A., Torregrosa I., Martí J. M., Gómez J. L., Perucho M., 2021, A&A, 650, A61
Hanawa T., Okoda Y., Yang Y.-L., Sakai N., 2025, ApJ, 986, 150
Hansen E. C., Frank A., Hartigan P., 2015, ApJ, 800, 41
Hillel S., Schreier R., Soker N., 2022, MNRAS, 514, 3212
Kossl D., Muller E., Hillebrandt W., 1990, A&A, 229, 401
Lei Z. et al., 2024, Commun. Phys., 7, 107
Lind K. R., Payne D. G., Meier D. L., Blandford R. D., 1989, ApJ, 344, 89
Mandal S., Duffell P. C., Li Y., 2022, ApJ, 935, 42
Martí J. M., Perucho M., Gómez J. L., 2016, ApJ, 831, 163
Mignone A., Bodo G., Massaglia S., Matsakos T., Tesileanu O., Zanni C., Ferrari A., 2007, ApJS, 170, 228
Mizuno Y., Gómez J. L., Nishikawa K.-I., Meli A., Hardee P. E., Rezzolla L., 2015, ApJ, 809, 38
Norman M. L., Winkler K.-H. A., Smarr L., Smith M. D., 1982, A&A, 113, 285
Obonyo W. O., Lumsden S. L., Hoare M. G., Purser S. J. D., Kurtz S. E., Johnston K. G., 2019, MNRAS, 486, 3664
Pudritz R. E., Hardcastle M. J., Gabuzda D. C., 2012, Space Sci. Rev., 169, 27
Pulatov V., 2001, Progr. Aerospace Sci., 37, 245
Rawlings S., Jarvis M. J., 2004, MNRAS, 355, L9
Richards C., Smith M. D., 2024, MNRAS, 532, 1929
Rubini F., Lorusso S., Del Zanna L., Bacciotti F., 2007, A&A, 472, 855
Silk J., Rees M. J., 1998, A&A, 331, L1
Smith M. D., 2012, Astrophysical Jets and Beams. Cambridge Univ. Press, Cambridge
Smith M. D., Keogh T. L. R., 2022, MNRAS, 516, 2757 (SK22)
Smith M. D., Richards C., 2023, MNRAS, 526, 3407

Smith M. D., Norman M. L., Winkler K.-H. A., Smarr L., 1985, MNRAS, 214, 67
Smith M. D., Ramachandran B., Krishna K., Jyothy S. N., 2025, MNRAS, 541, 3412
Suzuki-Vidal F. et al., 2011, Ap&SS, 336, 41
Tam C. K. W., 1995, Ann. Rev. Fluid Mech., 27, 17
Teşileanu O., Mignone A., Massaglia S., 2008, A&A, 488, 429
Velović V. et al., 2022, MNRAS, 516, 1865
Wang J.-S., Reville B., Mizuno Y., Rieger F. M., Aharonian F. A., 2023, MNRAS, 519, 1872

This paper has been typeset from a TEX/LATEX file prepared by the author.